The Journal of Chemical Physics

Accurate Non-bonded Potentials based on Periodic Quantum Mechanics Calculations for use in Molecular Simulations of Materials and Systems

Saber Naserifar[1], Julius J. Oppenheim[1], Hao Yang[1], Tingting Zhou[1,2], Sergey Zybin[1], Mohamed Rizk[1], and William A. Goddard III[1]*

[1]*Materials and Process Simulation Center, California Institute of Technology, Pasadena, California 91125, United States*

[2]*Institute of applied physics and computational mathematics, Fenghao Donglu, Haidian District, Beijing, 100094.*

**corresponding author: wag@caltech.edu*

Abstract

Molecular dynamics simulations require accurate force fields (FF) to describe the physical and chemical properties of complex materials and systems. FF parameters for valence interactions can be determined from high-quality Quantum Mechanical (QM) calculations. However, it has been challenging to extract long-range non-bonded interaction potentials from QM calculations since there is no unambiguous method to separate the total QM energy into electrostatics (polarization), van der Waals (vdW), and other components. Here, we propose to use DFT with dispersion corrections to obtain the equation of state for single element solid systems (of H, C, N, O, F, Cl, Br, I, P, He, Ne, Ar, Kr, Xe, and Rn) from which we obtain the pure 2-body vdW non-bonded potentials. Recently, we developed the polarizable charge equilibration (PQEq) model based on QM polarization energy of electric probe dipoles with no contributions from vdW. Together, the vdW and PQEq interactions form the non-bonded potential of our new transferrable reactive FF (RexPoN). They may also be useful to replace the non-bonded parts of standard FFs, such as OPLS, Amber, UFF, and CHARMM. We find that the individual 2-body vdW potential curves can be scaled to a universal vdW potential using just three specific atomic parameters. This simplifies extension to the rest of periodic table for atoms that do not exhibit molecular packing. We validate the accuracy of these non-bonded interactions for liquid water, energetic, and biological systems. In all cases, we find that our new non-bonded potentials provide good agreement with QM and experimental data.

I. Introduction

Molecular dynamics (MD) simulations have become an essential partner with experiment, playing a major role in elucidating physical and chemical properties of systems and in developing new generations of materials. Ideally one would use QM methods to make the most accurate predictions of the properties of new systems. However, QM methods are computationally limited to hundreds of atoms for dozens of picoseconds, which is inadequate for most developments of new generations of catalysts, materials, and pharmaceutical molecules, particularly for electrochemical and biological systems where explicit description of solvent is important. A system just 25 nm on a side already requires millions of atoms for time scales of microseconds or more, far beyond the realm of QM. Thus, we need to develop FFs that retains the accuracy of QM while scaling to millions of atoms and microseconds.

Most FFs distinguish between short range valence interactions and long-range non-bonded interactions. The valence interactions may be cast in terms of bond distances, angles, torsion, and inversion terms. The long-range non-bonded interactions include electrostatics, polarization, and van der Waals (vdW) terms (which account for London dispersion and Pauli repulsion). In addition, hydrogen bond (HB) corrections are often needed to describe short-range corrections to the non-bonded interactions.

Many FFs have been developed for simulations of various systems including biological systems (OPLS[1], AMBER[2], CHARMM[3]), water (TIP4P-2005[4], mW[5], SPC/Ew[6], and TIP3P[7]), membranes[8,9], energetic materials[10], and catalytic reactions[11,12]. Some of these FFs are generic (e.g. UFF[13]), and some can describe bond breaking and reactions (e.g. ReaxFF[14]).

FFs use a variety of functional forms for the non-bonded potentials, including the Lennard Jones (LJ) 12-6 (AMBER[2], OPLS[1], DREIDING[15], CHARMM22[3], GROMOS[16]), Buckingham exponential-6 and its modified version (MM2[17], MM3[18], DREIDING X6[15], APPLE&P[19]), and buffered 14-7 (MMFF[20], AMOEBA[21]).

The quality of these FFs depends mainly on the accuracy of the parameters, particularly beyond the training set.

Mainly two approaches have been used to determine the parameters of the non-bonded potentials. In the first approach, the parameters of the potentials are fitted to reproduce one or more experimental properties. For example, empirical water FFs (e.g. TIP4P-2005, and SPC/Ew) were developed by fitting the parameters of the models to reproduce two or more experimental properties such as density, heat of vaporization, diffusion, and/or melting point. Biological FFs such as OPLS, AMBER, and CHARMM FFs often focused on properties of proteins or nucleic acids. A major problem of such FFs is that their parameters are based on reproducing experimental quantities for specific systems, limiting their accuracy for novel systems. See references[22,23] for a comparison between the accuracy of different water models that are fitted to reproduce different experimental properties.

The second approach uses QM based data to optimize parameters. This may provide potentials with more accurate descriptions of chemical and physical interactions at the atomistic level. Also, it makes the FF more suitable for novel systems under conditions not accessible to experiment. However, the quality of QM based FFs depends highly on level of QM and how this data is used to optimize the FF parameters.

Usually, the QM data for relatively small molecular structures are used for parameter fitting. For example, the MB-pol[24] and CC-pol[25] ab-initio based water models were developed by fitting potentials and many-body terms to a large data set of water dimers and trimers using high quality QM data.

The QM data for such small non-periodic molecular structures may not sample the long-range interactions important in multi-scale simulations of bulk materials.

Sometimes, the FF parameters are extracted from QM calculations on crystals (periodic systems) by fitting to quantities such as bulk moduli, elastic constant, and lattice parameters. Then, the parameters of the non-bonded potentials are optimized together to agree with QM. Here, the problem is for systems containing several atomic types there is not a clear methodology to separate the contributions of vdW, electrostatics, and polarization terms from the QM. Thus, such FFs may

perform well only for the particular system that was fitted to but are often not transferable to new systems.

Some FFs (e.g. Amber and OPLS) use QM partial atomic charges as the reference data points to establish the electrostatics energy term separately[26]. The problem here is that the electron population analysis (EPA) to convert the QM electron density to partial atomic charges is ambiguous. Many EPA methods are used, including Mulliken population analysis (MPA)[27,28], Löwdin population analysis (LPA)[29,30], and electrostatic potential (ESP)[27]. These methods sometimes result in very different atomic charges for similar molecular structures (see reference[31] for more details). Therefore, the value and quality of the electrostatic energy term are significantly affected by quality of QM based partial atomic charges. Some FFs (e.g. CHARMM) use the ab-initio dipole moments of molecules to obtain the fixed atomic charges. Here, the use of fixed charges avoids molecular charge distribution to be updated based on the changes in the electrostatic environment.

Our goal is to develop a new strategy that allows us to separately define different components of the non-bonded potential based on accurate periodic QM (energy or forces) calculations.

For the electrostatic interactions we use our recent polarizable charge equilibration (PQEq) model[8]. PQEq uses an atomic sized Gaussian shaped electron density (not point charges) that can polarize away from the core (using a Gaussian function to describe the shell) in response to internal and external electric fields. The atomic charges are updated dynamically to achieve a constant chemical potential across all atoms in the system. An important feature of PQEq is that all atomic parameters are validated by comparing to QM interaction energy (not the partial charges) allowing validation using electric probe dipoles are scanned along different directions for molecular structures[31–33]. Here, the interaction energy includes only electrostatics and polarization effects which helps to optimize *directly* the parameters of PQEq based on QM data.

Next, we need to develop a methodology to describe the vdW interactions based on accurate DFT methods. We found that DFT including the Grimme[34,35] vdW or London dispersion corrections (D2 and D3), leads to energy-volume equations of state (EOS) for molecular solids in good agreement with experiment[23]. Thus, we report here the two-body non-bonded interaction parameters based on fitting to the QM EOS for several main group single element crystals including H, C, N, O, F, Cl, Br, I, P, He, Ne Ar, Kr, Xe, and Rn elements. We consider that these parameters capture the pure vdW interactions since the electrostatic and polarization contributions are negligible for these molecular systems (see Discussion section).

Together, the vdW and PQEq interactions provide the long range or non-bonded part of our new generation reactive FF[23] (RexPoN). RexPoN uses QM optimized polarization (Po), QM based non-bonded (N), and QM based bond dissociation (Rex). For systems such as water and biological systems we allow explicit hydrogen bond (HB) term to tune the short range non-bonded interaction (see Applications section). This paper does not discuss PQEq and the valence interactions, the details of which are provided in our previous publications.[23,31–33]

The present study focuses on the development of the vdW non-bonded potentials using the EOS of the single element crystals. For simplicity we refer to this as the "non-bonded" interactions.

Thus we determined the individual two-body non-bonded potentials for each of the 15 above elements by fitting to the energy-volume EOS data (called $E_{PR\text{-}LD}$). These fittings make no

assumptions about the functional form (e.g., LJ, Morse, or Buckingham). Rather we use a general Rydberg expansion to provide the best fit to the reference data.

We discovered that scaling the non-bonded potential curves of the noble gases by normalizing the well depth energy (D_e), bond distance (R_e), and curvature using a scaling length (L) led to nearly identical scaled potentials. Having such a universal non-bonded potential requiring only three parameters for each element would be most valuable for extending non-bonded interactions to the rest of the periodic table for elements that do not lead to molecular crystals. Thus, we define a universal non-bonded potential (E_{UNB}) by averaging the individual scaled potential for each of the 6 noble gas atoms. For all 15 elements we have extracted the D_e, R_e, and L that fits E_{UNB}.

This paper is organized as follows. Section II describes the crystal structures and energy-volume EOS calculations for 15 main group elements. Section III provides the details of fitting EOS to the non-bonded potentials. Section IV details the derivation of the universal non-bonded potential, which can be the starting point for the remaining elements of the periodic table. Section V discusses our methodology. Section VI reports the application of RexPoN to several systems. The conclusions are given in Section VII.

II. Crystal Structures and Energy-Volume Equation of States (EOS)

We used DFT-D3 QM to computed the energy-volume EOS of some of the main group elements including H, C, N, O, P, halogens (F, Cl, Br, I), and noble gases (Ne, He, Ar, Kr, Xe, and Rn). For all cases, we started from the most stable crystal structures obtained from the literature. Then, we changed the volume of the cells to calculate the single point energies versus volume. For cases with bonds, we fixed the bond distances and angles to avoid contributions from valence terms. We compressed the cells to small volumes to obtain the short-range non-bonded interactions corresponding to high pressures (above 100 GPa). Here, we provide a short description of each system.

Hydrogen. X-ray diffraction shows that the H_2 crystal has hexagonal closed packed structure with the *P6₃/mmc* space group and *c/a* ratio close to the ideal value of 1.633[36]. However, since hydrogen has no core electrons, X-ray experiments cannot determine the exact position of the H atom coordinates. Therefore, extensive theoretical studies have been carried out to determine the H_2 molecule orientation. It was found that the *Pca2₁* space group (see Figure 1) containing a hexagonal close packed structure with four molecules per unit cell is the most stable structure at high pressure ranges (~110-150 GPa)[37,38]. The equilibrium bond distance of H-H is 0.74 Å.

Oxygen. For solid oxygen, we selected the stable α-phase crystal structure, which according to neutron-diffraction and X-ray measurements has monoclinic base-center structure with *C2/m* space group[39,40] and O-O bond distance of 1.207 Å.

Carbon. To compute the EOS of carbon, we used the alpha hexagonal structure of graphite with the *P6₃/mmc* space group (ABAB stacking sequence).[41] The hexagonal rings in the plane are covalently bonded with the C-C bond lengths of 1.424 Å.

Nitrogen. We selected two systems for nitrogen crystals. The first structure is the alpha-N_2 structure that exists below 35.6 K with the Pa3 space group.[42] The bond distance of N_2 molecules is 1.112 Å. The second structure is the black phosphorous structure (see below) where we replaced the phosphorus atoms with nitrogen. The reason for including this structure is to examine the non-bonded interactions between nitrogen atoms that have single bonds rather than a triple bond.

Phosphorus. The stable black-phosphorous (BP) structure is orthorhombic with *Cmca* space group. The BP structure is stable at ambient conditions.[43] The crystal structure consists of interconnected six-membered rings with 2.256 and 2.227 Å bond distances.

Halogens. For fluorine, we used the crystal structure of α-F determined by X-ray powder diffraction at 23 K with *C2/c* space group[44] and the F-F bond distance of 1.45 Å. For chlorine, bromine, and iodine, we used the crystal structures determined by neutron diffraction at low temperatures which have *Cmca* space groups. We used solid crystals of Cl_2 at 22 K[45] for Cl, Br_2 at 5 K[45] for Br, and I_2 at 15 K[46] for I. The bond distances in the cells are 2.01 Å for Cl_2, 2.30 Å for Br_2, and 2.72 Å for I_2.

Noble gases. All the noble gas crystal structures were produced by scaling the cell size of a face-centered cubic structure, which is known to be the most stable form for noble gases crystals.[47]

The crystal structures of H, C, N, O, P, F, Cl, Br, and I systems are shown in Figure 1.

The DFT-D3 energy-volume EOS are shown in Figure 2 for H, C, N, O, and P elements, in Figure 3 for halogens, and in Figure 4 for noble gases (black open circles). The solid red lines show the fitting of RexPoN non-bonded potentials to the DFT-D3 data as described in the next section.

To avoid any contribution from changes in the covalent bonds, we kept all bond lengths and angles fixed at the value for the stable/equilibrium structure. To compute the energy for each volume, we subtract the total energy of the cell from the reference molecule with the same bond lengths and angles in all cells. See Supplementary Materials (SM) for more details.

We calculated the EOS for all systems using Perdew–Burke–Ernzerhof (PBE)[32] flavor of DFT. The only exception is for solid oxygen crystal which we used Becke, three-parameter, Lee-Yang-Parr (B3LYP)[48,49] including the hybrid terms important for describing the O_2 $^3\Sigma_g^-$ triplet state[35, 36], which is poorly described by PBE. See more discussion about the EOS of O_2 in reference[23]. To account for long-range vdW interactions we used DFT-D3 Grimme dispersion correction with the Becke-Johnson parameters[35,50]. See SM for more information about DFT-D calculations.

The cell volumes were scaled isotropically for all noble gases, H, N (alpha), and O crystals. For C, F, Cl, Br, and I we changed the cells along the direction perpendicular to the molecular planes while for P and N (BP) we changed the cells along *b* direction. The valence bonds and angles were kept fixed during the EOS calculations.

We compressed the volumes of the cells to achieve pressures up to 120 GPa for H, 315 GPa for C, 332 GPa for N (440 GPa for N in the BP structure), 300 GPa for O, 194 GPa for P, up to 440 GPa for halogens, and up to 2000 GPa for noble gases.

III. Fitting the Non-bonded Potential

We fitted two body vdW non-bonded interaction functions to the computed energy-volume EOS from DFT-D. Our non-bonded potential is defined to capture general repulsive interaction arising from the Pauli Principle (also referred to a vdW repulsion), denoted here as PR, and the attractive interactions arising from London dispersion (or vdW attraction), denoted here as LD. For PR we use a combination of two exponential terms and for London dispersion we use a low-gradient (LG) functional form as was proposed by Liu and Goddard[51] and used in the LD corrections to DFT by Kim *et al.*[52] The sum of the PR and LD terms forms our non-bonded potential (PR-LD),

$$E_{PR-LD} = E_{PR} + E_{LD} = \sum_{i<j} A_{ij}\exp(s_{ij}r_{ij} + \beta_{ij})\exp\left(\gamma_{ij}r_{ij}^{n_{ij}} + \eta_{ij}r_{ij} + \delta_{ij}\right)Tap(r_{ij}) - \sum_{i<j}\frac{C6_{ij}}{r_{ij}^6 + R_{vdWij}^6}Tap(r_{ij}), \quad (1)$$

where, r_{ij} is the interatomic distance. The first sum is designed to be monotonic purely repulsive (positive) term with A_{ij}, s_{ij}, β_{ij}, γ_{ij}, n_{ij}, η_{ij}, δ_{ij} being adjustable parameters. The second sum is a monotonic attractive term with $C6_{ij}$ the dispersion energy parameter and R_{vdWij} the equilibrium vdW distance between atoms i and j. This term goes as $1/r_{ij}^6$ for long r_{ij} but has an inflection point at R_{vdWij} becoming constant and small for normal bond distances. All of the parameters in Equation 1 depend only on the atomic types.

The $Tap(r_{ij})$ is a *7-th* order taper function with a finite range which is used to screen the non-bonded interactions. The taper function makes the non-bonded potential energy and its first three derivatives go smoothly to zero at a finite distance,

$$Taper(r_{ij}) = \sum_{m=0}^{7} Tap_m\left(\frac{r_{ij}}{r_{cut}}\right)^m \quad (2)$$

Here r_{cut} is a cutoff length (12.0 Å) and $Tap_7 = 20$, $Tap_6 = -70$, $Tap_5 = 84$, $Tap_4 = -35$, $Tap_3 = 0$, $Tap_2 = 0$, $Tap_1 = 0$, and $Tap_0 = 1$.

We used a step-by-step optimization strategy to obtain the parameters in Equation 1. We performed the parameter optimization for each atomic type separately. We constructed the training set by subtracting the total DFT-D energy of the crystals (for every volume along the EOS curve) from the energy of the reference structure. See section 2 of the SM for more details about reference structures. Throughout the optimization we minimized the error (cost) function given by

$$Error = \sum_{i=0}^{N_t}\frac{1}{w_i^2}(E_{DFT-D} - E_{PR-LD})^2 \quad (3)$$

Where N_t is the number of items in the training set and w_i is the weight for each data point in the training set.

We started with the E_{LD} term (second sum in Equation 1) and used the initial values for R_{vdWij} and $C6_{ij}$ from the Universal Force Field (UFF) (available up to lawrencium, Z = 103)[13]. Our initial goal is to modify these two parameters in such a way that the value of the E_{LD} term becomes twice as deep as the DFT-D value at the volume corresponding to the well depth (V_w) of EOS (i.e. $E_{LD} = -2E_w$ at V_w). The DFT-D value for the total binding leads to $-E_w$, which is the sum of a positive PR term and the London Dispersion. We assume that at V_w the E_{LD} is $-2E_w$ and the E_{PR} is $+E_w$.

Since the UFF values for R_{vdWij} are reasonably accurate, we modified only the $C6_{ij}$ parameter (defined based on atomic polarizabilities in UFF) to satisfy this condition. However, we optimize parameters in later steps so the final values for R_{vdWij} and $C6_{ij}$ may differ from the starting parameters.

Next, we performed the optimization of A_{ij}, s_{ij}, and β_{ij} in the first exponential term of E_{PR}. Our goal here is to minimize the cost function in Equation 3 to get the best fit. Once reasonable agreement is obtained to the reference values, we turn on optimization of the parameters in the second exponential term (γ_{ij}, n_{ij}, η_{ij}, and δ_{ij}) to improve the quality of the fit. Here, the quality of the E_{PR} energy term is mainly controlled by the first exponential term. In some cases, we obtained the final parameters just by optimizing the E_{LD} term and the first exponential term of E_{PR}. Finally, we performed a global optimization (when needed) of all parameters together to further minimize the value of the cost function.

There are two important reasons in using the above step-by-step optimization strategy. First, it helps to avoid over-fitting of the parameters. Thus, the parameters obtained are not biased toward the training set and have better global character. Second, it helps to define more physical repulsive and attractive energy curves rather than just trying to reduce the value of cost function.

Initially, we used w_i=1 for all data points in the training set. However, during the global optimization step we assigned smaller w_i values to the training data points around the well depth to increase the accuracy of the fit around the equilibrium. Here we varied the value of w_i from 0.1 to 1.0. More details about the optimizer engine are provided in the SM.

The fits for the above elements are shown in Figure 2 to Figure 4 (solid red lines). We find an excellent fit for all cases. Therefore, the $E_{PR\text{-}LD}$ of RexPoN provides a description of the short- and long-range non-bonded interaction for each element at the accuracy level of DFT-D3. The optimized parameters of $E_{PR\text{-}LD}$ are provided in Table 1.

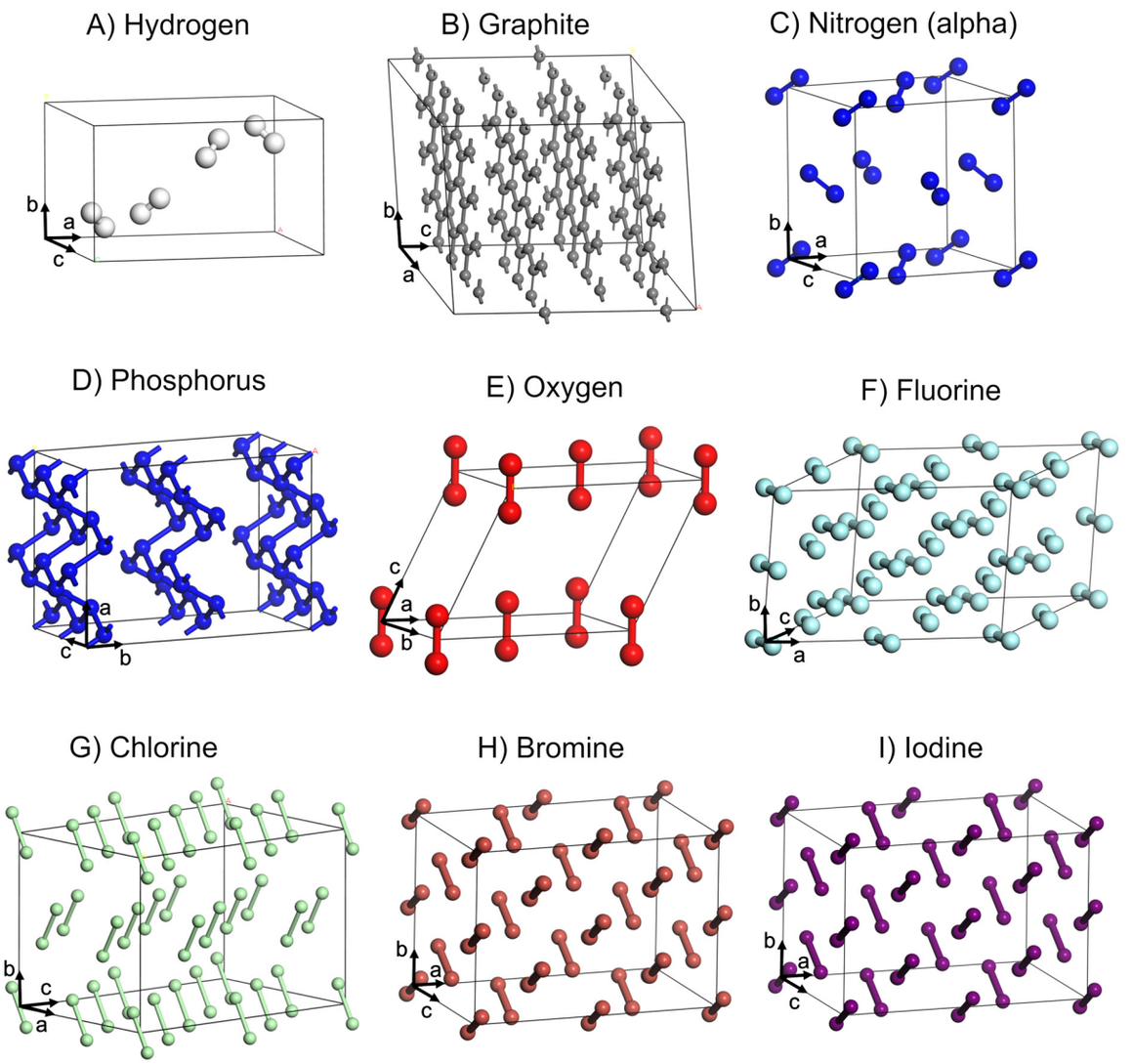

Figure 1. Crystal structures of A) hydrogen, B) graphite, C) nitrogen (alpha phase), D) black phosphorous (BP) (also used for nitrogen BP) , E) oxygen, F) fluorine, G) chlorine, H) bromine, and I) iodine. Supercells are included in B, D, F, G, H, and I in order to show the molecular structures better.

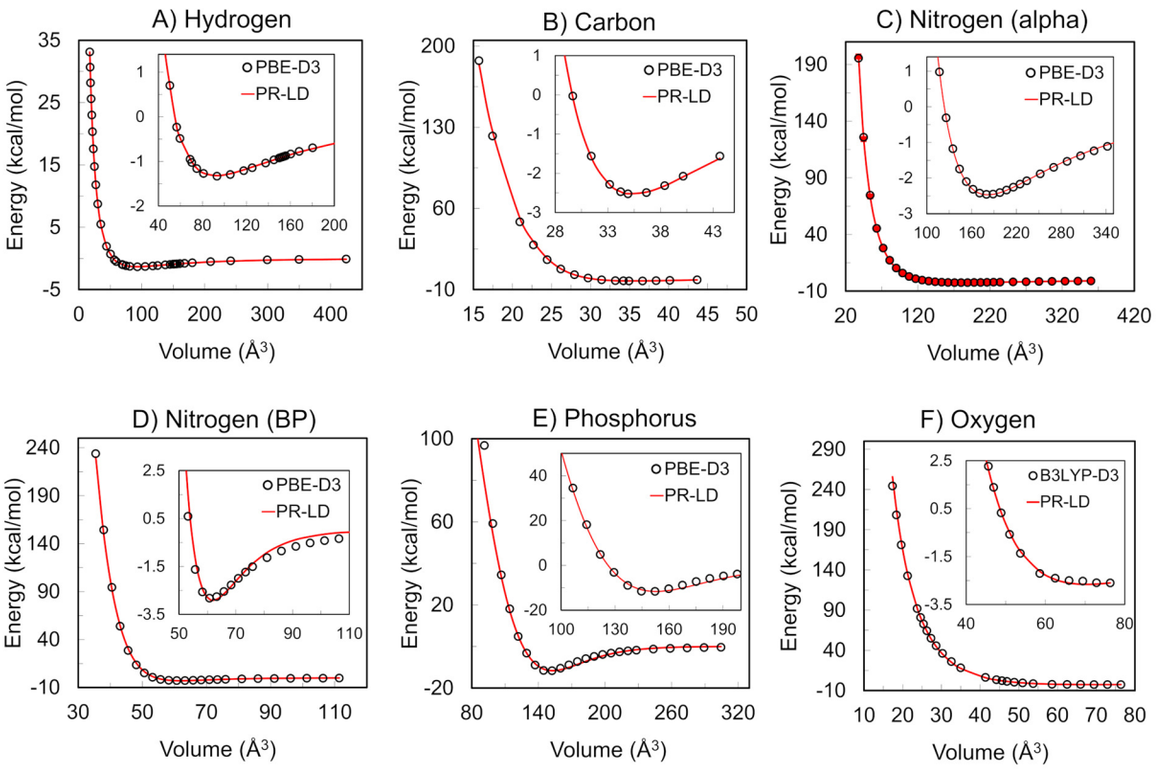

Figure 2. The vdW energy-volume EOS computed by DFT-D3 and RexPoN for solid A) hydrogen, (B) graphite, C) nitrogen (alpha phase), D) nitrogen (black-phosphorus structure), E) black phosphorus, and F) oxygen. The two-body $E_{PR\text{-}LD}$ non-bonded potential function given in Equation 1 (red line) was fitted to each DFT-D to obtain the adjustable parameters. These parameters are listed in Table 1.

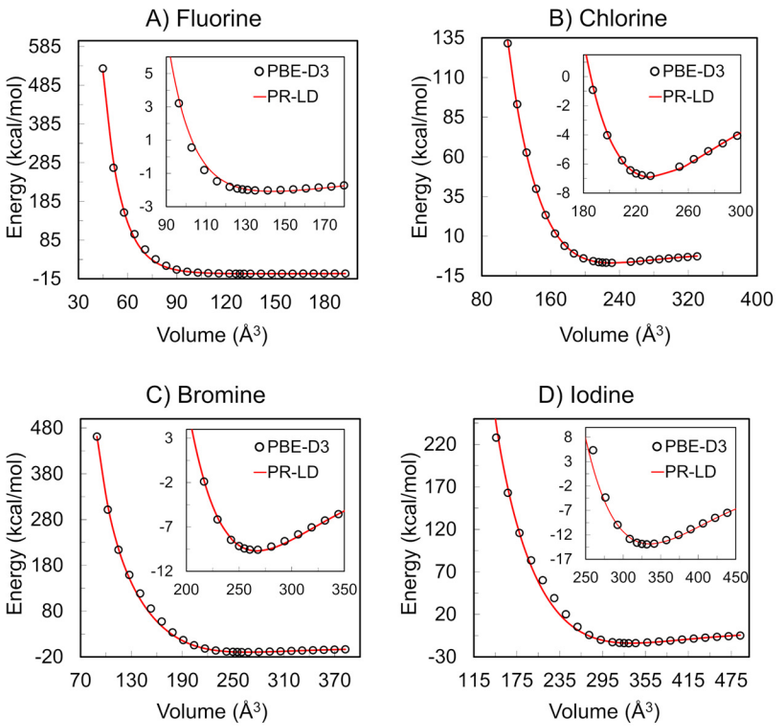

Figure 3. Same as Figure 2 but for halogen atoms including solid A) fluorine, B) chlorine, C) bromine, and D) iodine.

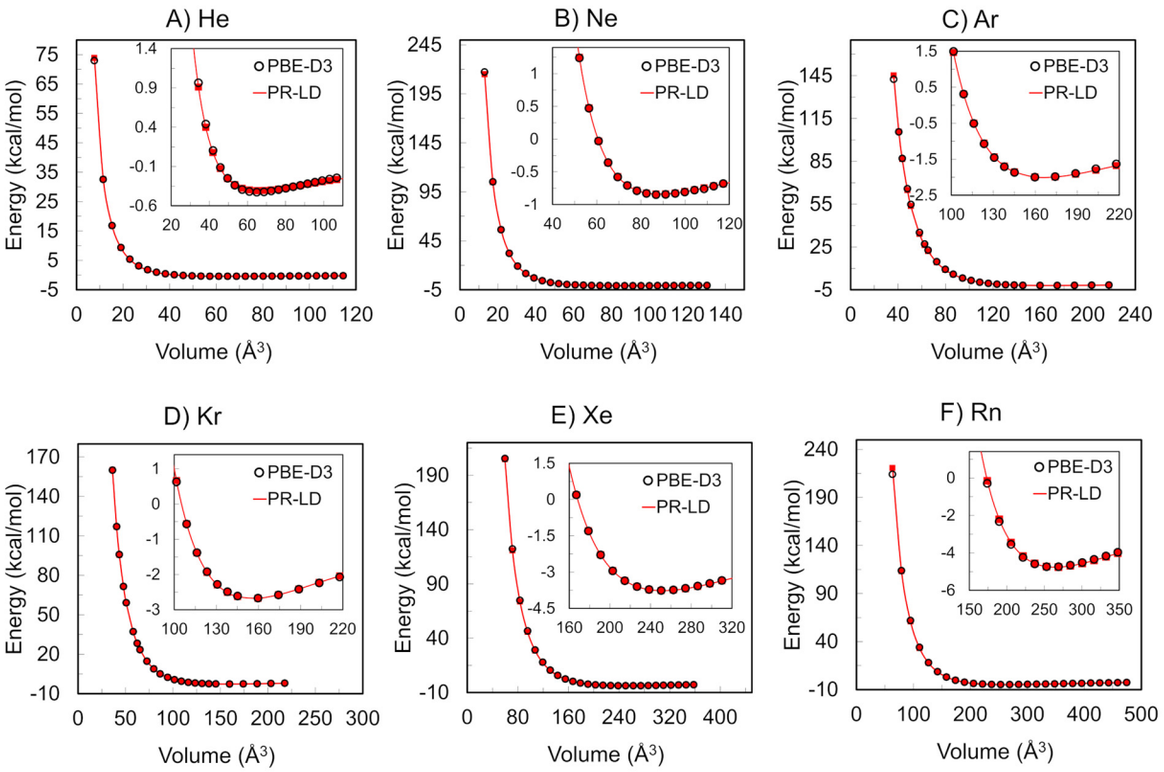

Figure 4. Same as Figure 2 but for noble gases including A) He, B) Ne, C) Ar, D) Kr, E) Xe, and F) Rn.

Table 1. Parameters of non-bonded potential energy term ($E_{PR\text{-}LD}$) given in Equation 1.

Atom	*A*	*s*	*β*	*γ*	*n*	*η*	*δ*	*RvdW*	*C6*
H	0.0212	-2.4002	10.5460	-0.8113	0.0014	-0.2607	-0.5640	1.6346	239.4803
He	0.0143	-3.5531	11.7112	0.0000	1.0000	0.0000	0.0000	1.1937	87.9969
C	0.2537	-2.4545	1.8207	0.3108	0.8248	-0.4569	7.7134	1.3400	792.9588
N (alpha)	0.3670	-3.7952	5.5977	4.4641	0.4424	0.0010	0.0010	1.1781	1000.9191
N (BP)	8.4296	-2.9375	6.8368	-0.0004	0.6089	0.0010	-0.0008	1.0564	593.9540
O	0.0272	-3.6468	14.5278	-0.3235	0.0305	0.0331	-0.5688	1.4969	634.7066
F	0.7710	-3.9612	10.0284	0.0286	2.8974	0.1941	-0.0086	1.6762	921.9329
Ne	0.1048	-4.0308	12.4882	0.0029	0.9966	0.0163	0.0423	1.3518	291.8884
P	3.6525	-2.0073	6.7334	-0.4335	0.5155	0.5514	-1.3245	2.0000	13000.0000
Cl	3.4737	-2.6483	8.4472	0.1872	0.6288	0.0124	-0.3986	1.4241	3680.2392
Ar	2.2852	-3.1609	9.8446	0.0027	0.9965	-0.0136	0.0482	1.9108	3425.3776
Br	5.7482	-1.5770	4.7932	-0.0783	1.2980	-0.4349	2.1154	1.6561	8502.2025
Kr	10.4740	-2.8331	8.2831	0.0002	1.0000	0.0001	-0.0001	1.9195	6579.6328
I	1.7070	-2.3274	9.1643	-0.5343	0.5218	0.1545	0.4811	2.2828	22100.0000
Xe	14.2394	-2.6297	8.2880	1.4575	0.7617	-0.9165	-0.6258	2.2992	18800.6328
Rn	16.0833	-2.6363	8.4742	0.0000	1.0000	0.0000	0.0000	2.4949	33000.0000

IV. Universal Non-bonded Potential Function

The EOS of noble gases provides pure non-bonded interactions since there are no valence or electrostatic interactions.

In order to analyze the functional form for these non-bonded vdW interactions, we use the same scaling methodology proposed by Rose *et al.*[53]. We scale the curves such that at the minimum position of the potential well (R_e) the dimensionless values of energy and second derivative (i.e. curvature) are both equal to one. Therefore, we use the well depth energy (D_e), R_e, and a scaling length parameter (L) and set

$$\rho = \frac{R - R_e}{L}, \tag{4}$$

$$\varepsilon = \frac{E}{D_e}, \tag{5}$$

and

$$\frac{\omega L^2}{D_e} = 1 \tag{6}$$

where ω is the curvature or the value of the second derivative of the potential curve at R_e (at $r = R_e$, $\omega = d^2E/dr^2$). Equation 6 is used to determine the value of L which makes the dimensionless curvature at ρ equal to 1. We use the $E_{PR\text{-}LD}$ two-body potential energy curves to obtain the atomic parameters (R_e, D_e, and L) for each element. The atomic parameters are listed in Table 2. Using Equations 4 to 6, the scaled two-body potential energy curves are shown in Figure 5B. We note that the scaled curves are nearly identical (with a root mean square deviation in ε of 0.02 over the range ρ = -1.5 to 5), suggesting a universal non-bonded vdW potential that can be used for all elements of the periodic table. Using this universal curve, the two-body vdW interaction energy is defined by just the three parameters (R_e, D_e, and L) for each element. For interactions involving two or more elements, we use the geometric mean combination rules

We averaged all the scaled curved in Figure 5B to develop the universal scaled non-bonded curve which was then fitted to an extended Rydberg-type equation[54] given by

$$\varepsilon_{UNB}(\rho_{ij}) = -\exp(-\beta\rho_{ij}) \sum_{n=0}^{5} \alpha_n \rho_{ij}^n \tag{7}$$

where β and α_n are the universal parameters with the values provided in Table 3.

The scaled potential in Equation 7 can be converted back to the real space using the relations given in Equations 4 to 6 leading to the universal non-bonded potential (E_{UNB}) function given by

$$E_{UNB}(r_{ij}) = -D_e \exp\left[-\beta\left(\frac{r_{ij}-R_e}{L}\right)\right] Tap(r_{ij}) \sum_{n=0}^{5} s_n \left(\frac{r_{ij}-R_e}{L}\right)^n \quad (8)$$

We add a similar *7-th* order taper function as given in Equation 2 to screen the non-bonded interactions. Therefore, the non-bonded potential for any element can be obtained at the level of DFT-D with just the three parameters of the two-body non-bonded potentials.

This universal non-bonded curve should simplify estimating vdW non-bonded parameters for the elements of the periodic table which do not form molecular crystals dominated by vdW interactions (e.g. transition metals). Here we hope to extrapolate and interpolate the D_e, R_e, and L parameters to estimate unknown cases. Our goal is to provide an accurate universal potential (at the accuracy level of DFT-D) to describe the interatomic interactions for systems near equilibrium. As such, we chose the distances around the vdW potential well depth (ρ = -1.5 to 5). This helps avoid differences between non-bonded potential curves at very close distances on the E_{UNB}.

We have integrated both the $E_{PR\text{-}LD}$ and E_{UNB} functional forms into our local LAMMPS program software[55].

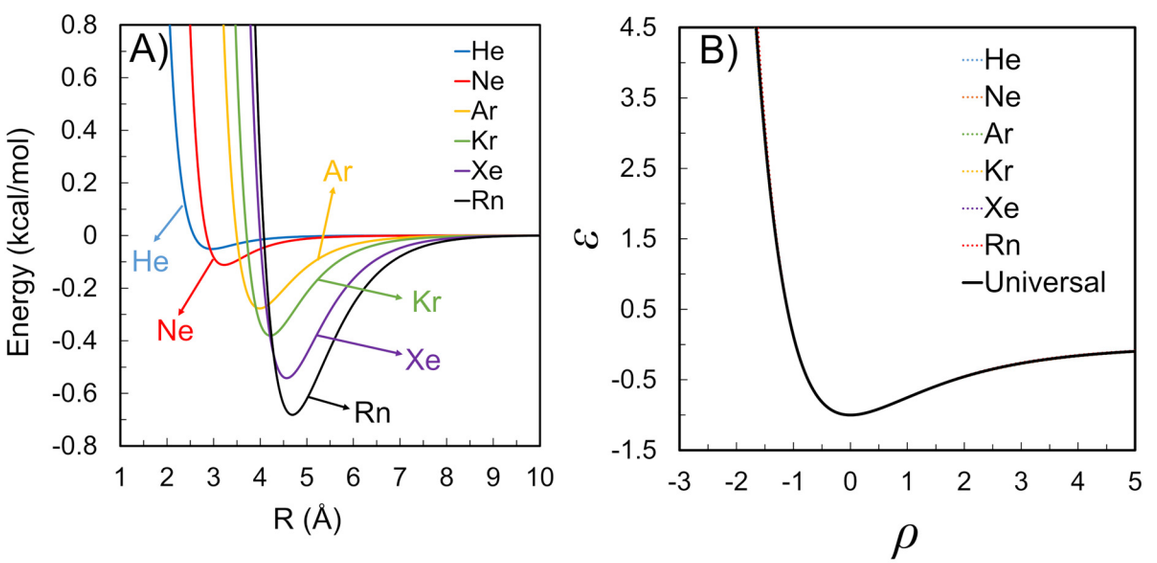

Figure 5. A) The two-body non-bonded or vdW potential energy curves of noble gas elements. B) The scaled energy curves obtained using the minimum well depth distance (R_e), energy (D_e), and the scaling length (L) using Equations 4 to 6.

Table 2. The R_e, D_e, and L atomic parameters obtained from two-body $E_{PR\text{-}LD}$ potential energy curves (Equation 1).

Atoms	R_e **(Å)**	D_e **(kcal/mol)**	L **(Å)**
H	3.2541	0.0528	0.5241
He	2.9752	0.0553	0.5241
C	3.9162	0.0971	0.5396
N (alpha)	3.8281	0.1456	0.5416
N (BP)	3.8918	0.0814	0.5170
O	3.4249	0.1498	0.4349
F	3.5018	0.1873	0.5199
Ne	3.2434	0.1229	0.4121
P	4.2238	0.6297	0.7194
Cl	4.0748	0.3500	0.5654
Br	4.3103	0.5143	0.6318
Ar	4.0336	0.3359	0.5604
Kr	4.2715	0.4790	0.5825
I	4.6316	0.8256	0.7161
Xe	4.6476	0.7316	0.6748
Rn	4.7938	0.9468	0.7464

Table 3. Parameters of the universal non-bonded energy curve (E_{UNB}) given in Equation 8.

β	α_0	α_1	α_2	α_3	α_4	α_5
1.0035	1.0000	1.0201	0.0168	0.0033	0.0037	0.0011

V. Discussion

Contribution of polarization energy to EOS. Our strategy is to use the computed EOS curve for single element crystals to define the non-bonded parameters in which electrostatic and polarization terms (described by PQEq) vanish. The PQEq model allows the charge distribution to change according to the electrostatic environment. The optimum charge distribution (q_i) and consequently the shell polarizations are computed from the conditions that the chemical potentials ($\partial E_{PQEq}/\partial q_i$) be equal for all atoms in the system and constraining the total charge of the system. Consequently, for a system in which all atoms are identical (i.e. same atomic type) the computed polarization energy by PQEq would be zero for a neutral system (zero atomic charges). More details about the charge and shell position calculations by PQEq is provided in reference [31].

Combination rules for the cross terms. We propose that for the cross term ($type_i \neq type_j$) interactions between two elements the geometric mean of the atomic parameters can be used ($D_{eij} = \sqrt{D_{ei}D_{ej}}$, $R_{eij} = \sqrt{R_{ei}R_{ej}}$, $L_{ij} = \sqrt{L_iL_j}$). To check the validity of this approximation, we computed the heat of vaporization (ΔH_{vap}) of noble gas crystals (A_nB_m) having different stoichiometric ratio of the atomic types (m:n = 1:3) using DFT-D3 and RexPoN. The results for the most stable volumes are provided in Table 5. The computed values by RexPoN are in reasonable agreement with DFT-D showing that the geometric mean provides accurate cross term parameters.

For mixed element systems calculations, we must include the PQEq electrostatics energy. Here we used the original PQEq parameters for noble gases[31]. The small differences between the values in Table 5 may arise from the use of the original PQEq parameters of noble gases, which have not yet been optimized using electric dipole scans.

Table 4. Comparison of heat of vaporization, ΔH_{vap} (kcal/mol), of noble gas crystals (A_nB_m) with various ratios of the atomic types (m,n = 1,3). Geometric mean average of the atomic parameters is used for cross term interactions.

	QM ΔH_{vap}	RexPoN ΔH_{vap}
He_1Ne_3	-0.73	-0.78
He_3Ne_1	-0.52	-0.64
Ne_1Ar_3	-1.56	-1.58
Ne_3Ar_1	-1.01	-1.30
Ar_1Kr_3	-2.45	-2.11
Ar_3Kr_1	-2.15	-1.90
Kr_1Xe_3	-3.31	-2.72
Kr_3Xe_1	-2.99	-2.39
Xe_1Rn_3	-4.31	-4.64
Xe_3Rn_1	-4.02	-4.27

Comparison of atomic parameters with UFF values. We compare the atomic parameters R_e and D_e derived from two body curves (Equation 1) with the UFF parameters[13] in Figure 6. In general, the D_e values of RexPoN follow a better trend across the rows and columns of periodic tables. Also, the D_e values of RexPoN are generally larger than UFF values (see the trends for halogens and noble gases). We find the R_e values of RexPoN and UFF to be close.

The dimensionless curvature of the E_{UNB} function (ω^*_{UNB}) is inversely proportional to L, ($\omega^*_{UNB} \propto 1/L^2$). See section 3 of the SM for more details. UFF uses both 12-6 Lennard-Jones (LJ12-6) potential and exponential 6 functions (exp6) for the vdW potential. Here LJ12-6 leads to $\omega^*_{LJ12-6} = 72$, whereas curvature is an additional parameter for exp6. In UFF optimized values were used for some atoms of the first two rows of the periodic table, but $\omega^*_{LJ12-6} = 72$ was used for the other elements.

However, for RexPoN the ω^*_{UNB} differ from one atom type to another. This gives the universal non-bonded function of RexPoN flexibility to define a more accurate vdW interaction for each element type.

In section 3 of the SM, we provide a detailed comparison of E_{UNB} potential with other well-known potentials including LJ12-6, Lennard-Jones 9-6 (LJ9-6), Morse, and the modified Buckingham exponential-6 (Be-6). In general, we find that the E_{UNB} is softer than LJ12-6 and LJ9-6 but stiffer than Morse and Be-6 potentials.

As mentioned earlier, we used two structures to determine the atomic parameters of nitrogen. We find that the D_e value of nitrogen with alpha structure to be larger than the black–phosphorus structure while the R_e and L values are quite close to each other.

The above comparisons suggest that for elements not studied here we can start with the UFF atomic parameters (available up to lawrencium, Z = 103) for the E_{UNB} function of RexPoN. However, DFT-D3 calculations should be performed for periodic cells of different atomic types and their combinations to develop accurate atomic parameters. The values of L can be extrapolated or interpolated across the rows or columns to provide a reasonable value for the elements not given here.

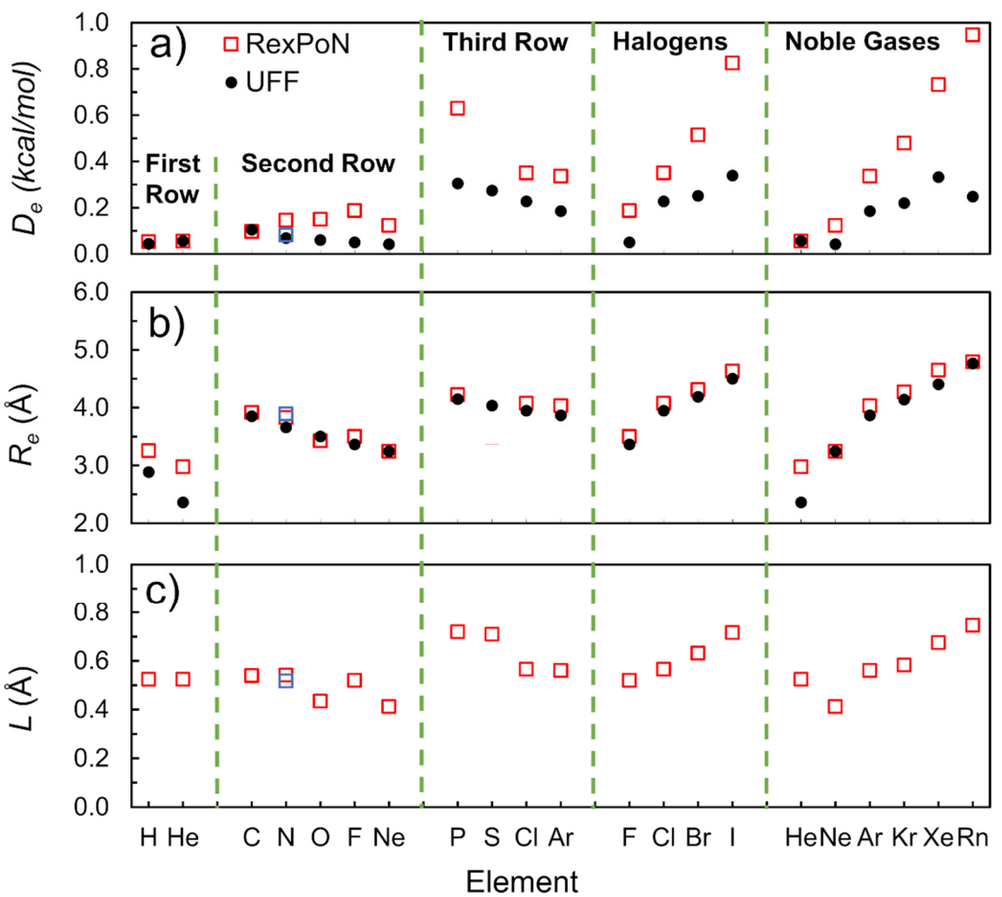

Figure 6. The trend of E_{UNB} potential atomic parameters for **a)** D_e, **b)** R_e, and **c)** L across the rows and columns of the periodic table. We compare the values of D_e and R_e with the UFF numbers. For nitrogen atom two series of values are provided for alpha-N_2 (red) and for nitrogen crystal with black-phosphorus type structure (blue).

Periodic versus non-periodic calculations. Rather than using the noble gas crystal, the noble gas pairwise non-bonded potentials can be determined from DFT-D3 on the noble gas diatomics. Figure 7 compares the two-body energy curves derived to fit the crystal EOS calculations with the diatomics computed using PBE-D3 energy with the cc-pVQZ(-g)++ basis set in the Jaguar

software (see section 1 of the SM). We find that the true two body interactions are deeper at shorter distances compared to those derived from the EOS. We see that the true two body interactions are larger at small distances that the ones derived from the EOS. The differences arise because the QM on the crystal includes 3-body vdW interactions (Axilrod-Teller)[56] that are repulsive. Thus, fitting the EOS to two-body interactions builds in some 3-body repulsion into the two-body interactions. We consider this to be useful in condensed systems where 3-body vdW interactions exist for all the atoms.

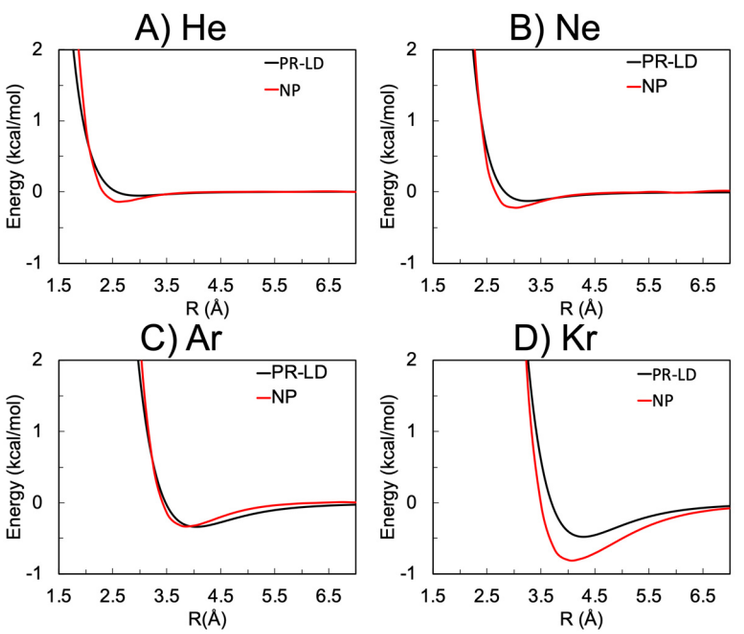

Figure 7. The two-body non-bonded potential energy curves of noble gas elements: A) He, B) Ne, C) Ar, and D) Kr derived from EOS ($E_{PR\text{-}LD}$) calculations on periodic system (black line) and directly by the scan of two atoms in a non-periodic system (E_{NP}) (red).

VI. Applications

In this section we use the RexPoN model for three applications to validate its accuracy. The first application uses the $E_{PR\text{-}LD}$ non-bonded term of RexPoN to compute the interfacial surface tension of liquid water at ambient temperature. The second and third applications use the E_{UNB} of RexPoN for five phases of the Cl-20 energetic material and Nelfinavir biological system.

Interfacial Surface Tension of Water. We first summarize the RexPoN FF for pure water[23]. RexPoN leads to the most accurate properties ever predicted by a FF for water, even though no empirical data was used. Thus, at 298 K RexPoN predicts[23]: heat of vaporization 10.36 kcal/mol (exp. = 10.52), density 0.9965 g/cm^3 (exp. = 0.9965), entropy 68.4 J/mol/K (exp. = 69.9), dielectric constant 76.1 (exp. = 78.4), and melting point 273.3 K (exp. = 273.15). RexPoN also reproduces the oxygen-oxygen radial distribution of the first coordination shell from neutron and x-ray scattering very accurately. Indeed, even DFT calculations do not reproduce this description of the first coordination shell of water.

Recently, we reported that MD simulations using the RexPoN reactive FF at 298 K finds an average of 2.1 Strong Hydrogen Bonds (SHB) with an average lifetime of τ_{SHB} = 90 fs.[22] We also reported that connecting these SHBs leads to a 1D polymer with occasional branches to sidechains. This established the revolutionary new DynPol paradigm for the structure of water as a dynamic polydisperse branched polymer, leading to an average cluster size of 151 at 298 K that decreases to 36 at 400 K. The average ΣSHB decreases from 2.1 down to 1.6 at 400 K, while τ_{SHB} decreases from 93 to 68 fs. The details of these simulations are described in reference [22].

As another indication of accuracy of our water force field we computed the interfacial surface tension of water (γ_s). The γ_s can be defined based on the free energy change that is required to change the surface area (A) of air-water interface by one unit when the system is under thermodynamic equilibrium (i.e. constant temperature T, pressure P, and number of molecules N),

$$\gamma_s = \left(\frac{\partial G}{\partial A}\right)_{N,T,P} = \left(\frac{G_s - G_b}{\partial A}\right)_{N,T,P}, \tag{9}$$

where G_s and G_b are the Gibbs free energy of the surface and bulk, respectively. This equation can be written based on entropy (S) and surface enthalpy (H) using Helmholtz free energy ($A=U-TS$) and Gibbs-Helmholtz ($G=A+PV$) equations,

$$\gamma_s = \left(\frac{H_s - H_b + TS_s - TS_b}{\partial A}\right)_{N,T,P} = \left(\frac{\Delta h_{ex} - T\Delta s_{ex}}{\partial A}\right), \tag{10}$$

where h_{ex} is molar excess surface enthalpy and s_{ex} is molar excess surface entropy.

To compute γ_s based on Equation 10 we use the two-phase thermodynamics (2PT) methodology[57,58]. 2PT allows for the direct calculation of absolute thermodynamics of the system based on the Fourier transform of the velocity autocorrelation function. The accuracy of 2PT for the calculation of thermodynamics of 2D slab geometries has been validated before[59].

We computed the γ_s of liquid water by performing two series of calculations. For the first calculation we utilized bulk water simulations at 298 K for a system with 432 molecules per cell. We first equilibrated the system at 298 K by running 0.6 nanoseconds (ns) constant volume, constant temperature (*NVT*) molecular dynamics (MD) simulations. To control the temperature we used the Langevin thermostat[60]. After this initial equilibration, we utilized 1.1 ns MD simulation using constant pressure (1 atm), constant temperature (*NPT*) ensemble to fully relaxed the simulation cell. Finally, we further equilibrated the system at 298 K for another 0.6 ns using *NVT* ensemble simulations. We saved the coordinates and velocities from the last 100 ps trajectories (5 cycles each 20 ps) every 1 femtosecond (fs) to perform 2PT calculations and compute γ_s.

For the second calculation, we started from the equilibrated bulk coordinates and velocities and performed 2D slab (surface) simulations at 298 K. We inflated the simulation cell of the bulk system in the z direction by about 6 nm and centered the slab within the cell allowing about 3 nm of vacuum at each surface of liquid (see Figure 8). We then performed *NVT* simulations of the

surface at 298 K for about 2 ns to equilibrate the system. Similar to bulk simulations, we used the trajectories from the last 100 ps to perform 2PT calculations.

For all of the above simulations we used the RexPoN rigid water model[23] with the time step of 1.0 fs. To control the pressure, we used a barostat with a relaxation time of 2 ps and to control temperature we used damping time of 100 fs.

We used 2PT to compute interfacial surface tension (γ_s) according to Equation 9 as,

$$\gamma_s = c\frac{G_s - G_b}{SA} \tag{11}$$

where c = 166.03 is the conversion which gives γ_s in dynes per centimeter and SA is the total surface area of both surfaces ($SA=2\times L_x\times L_y$). More details about the methodology to calculate interfacial surface tension using 2PT is provided in reference.[59]

Table 6 compares the experimental and computed interfacial surface tension (γ_s) of liquid water using RexPoN and some of the famous water models including TIP4P/2005[4], mW[5], SPC/Ew[6], and TIP3P[7]. The γ_s for these water models were computed by 2PT method and the data were taken from reference [59]. As shown, the RexPoN computed γ_s=69.5 dyn/cm is in great agreement with the experimental value of 71.9 dyn/cm.

Table 5. Comparison of experimental[61] and computed interfacial surface tension (γ_s, dyn/cm) of liquid water at 298 K. The computed γ_s for TIP4P/2005, mW, SPC/Ew, and TIP3P are from reference[59].

	Expt.	RexPoN	TIP4P/2005	mW	SPC/Ew	TIP3P
γ_s (dyn/cm)	71.9	69.5	64.4	66.9	55.8	52.6

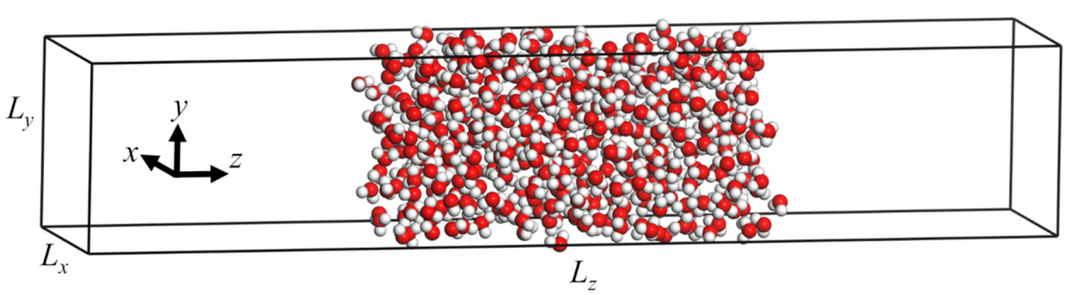

Figure 8. Snapshot of the air-water simulation cell showing 432 equilibrated water molecules at 298 K. The dimensions of the cell are L_x=L_y=1.86 nm, and L_z=9.70 nm. There is about 3 nm of vacuum on each surface in the z direction. The surface was relaxed at 298 K for about 2 ns using MD-*NVT* simulations with RexPoN FF.

High Energy Materials and Composites. It is crucial to predict the crystal structure of new energetic materials (EM) worthy of synthesis and characterization prior to the experiment[62,63]. EM have widespread applications in many areas including space exploration and mining. Predicting reliably the constitutive and chemical properties, as well as initiation kinetics processes that control stability, performance and sensitivity prior to synthesis and characterization is critical to the development of novel high-energy density materials (HEDM) and high-energy dense oxidizers (HEDO)[64].

The current classical FF with parameters fitted to empirical data are not sufficiently accurate for guiding the development of next generation EMs (see below), which may exhibit quite different crystal, constitutive, and reaction kinetics properties. To evaluate the accuracy of the RexPoN nonbond potential for different EM polymorphs, we choose a well-studied energetic crystal, hexanitro-hexa-aza-isowurtzitane (CL-20), for which five stable crystal polymorphs are known experimentally[65–67]: the α, β, ε, γ, and ξ phases shown in Figure 9.

First, we optimized the periodic crystal cell using PBE-D3 DFT to obtain the most stable structures within each phase. The dispersion-corrected DFT methods have been tested previously to predict experimental crystal structures and densities of EM to 1.6–2.1% maximum error for the lattice parameters[68]. After optimization, we estimated the sublimation energy at T=0 K ($\Delta_{0K}H_{sub}$) for each crystal phase by subtracting the total energy of the crystal from the energy of reference molecule outside of the corresponding cell. In the case of α–phase structure, the reference molecules are the α–CL-20 and water molecule. For other phases the reference molecule is taken from the corresponding phase of CL-20 crystal. Next, we calculated the $\Delta_{0K}H_{sub}$ using the RexPoN FF for the same crystal structures obtained from the PBE-D3 DFT optimization.

Here, the non-bonded interactions consist of vdW and electrostatic (including polarization) energies. For electrostatics we used PQEq model with the parameters optimized based on the electric dipole energy scans for cyclohexane-based molecular structures[31]. No EM molecules or structures were used to optimize the PQEq parameters. To provide a better understanding about the accuracy level of the RexPoN FF we also computed the $\Delta_{0K}H_{sub}$ for each of the above phases using the OPLS[69] FF developed to study biomolecular and condensed matter systems. We used the parameters from OPLS2005 FF[70] generated from the Desmond system builder[71].

The results are compared in Table 6. As shown, the RexPoN $\Delta_{0K}H_{sub}$ values for all phases are in much better agreement with the DFT-D3 calculations than OPLS FF. For the nitrogen parameters of RexPoN, we used the N parameters based on black phosphorus structure, N (BP), since it has bonding more similar to the N atoms in CL-20.

In terms of the ranking order for the heat of sublimation at 0 K, RexPoN and PBE-D3 find hydrated α–phase of CL-20 to be the most stable by $\Delta_{0K}H_{sub}$ = -47.2 and -48.7 kcal/mol, respectively. The $\Delta_{0K}H_{sub}$ value of RexPoN for the least stable ξ phase (-33.59 kcal/mol) is also quite close to the DFT-D value (-33.05 kcal/mol). For the β, γ, and ε phases both DFT and RexPoN find them within a range of 3 kcal/mol but slightly different ordering. This could be due to the fact that PQEq parameters were not optimized for energetic materials. Though no direct experimental measurements of the heat of sublimation for CL-20 polymorphs have been published, our results are in reasonable agreement with available experiment-based estimates (35.21–40.51 kcal/mol for

the sublimation on burning surface[72] and theoretical calculations (37.52±4.8 kcal/mol[73] and 40.32 kcal/mol[74]).

In contrast the $\Delta_{0K}H_{sub}$ from OPLS are too large by 11 to 23 kcal/mol

Table 6. Heat of sublimation at 0K, $\Delta_{0K}H_{sub}$ (kcal/mol), of various phases of CL-20 calculated with PBE-D3, RexPoN, and OPLS 2005 FF.

Phases	**PBE-D3**	**RexPoN**	**OPLS 2005**
α	-48.72	-47.22	-65.64
β	-35.63	-36.33	-52.54
γ	-37.06	-33.17	-48.12
ε	-35.52	-35.32	-54.10
ξ	-33.05	-33.59	-55.91

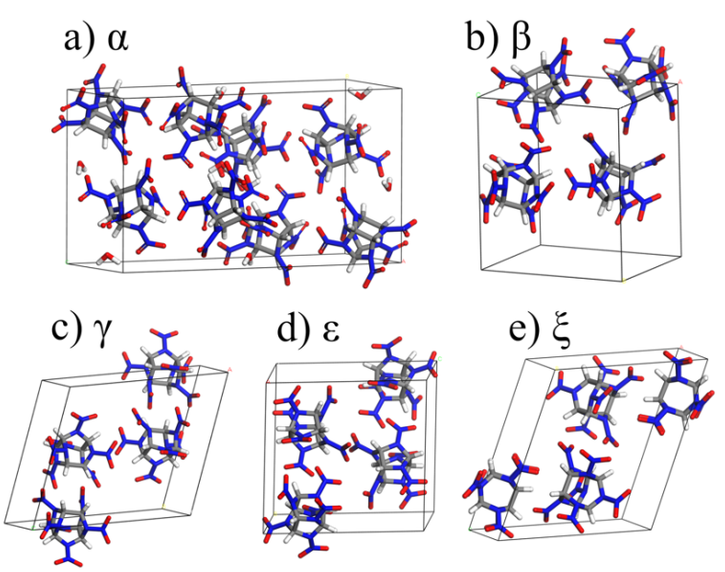

Figure 9. The crystal structure of (a) α-, (b) β-, (c) γ-, (d) ε-, (e) ξ-phase of CL-20 energetic material.

Biological Systems. A major challenge in rational drug design is the accurate prediction of drug-target interactions, which are predominantly noncovalent in nature.

Accurate QM-based methods are not practical since a protein with 400 amino acids, including water and ions may lead to 30,000 atoms. The available classical FFs are not generally sufficiently

accurate to obtain the desired accuracy for various drug-like molecules. One reason is that these FFs are often optimized for particular systems since it is difficult to find parameters fitting a wide range of compounds (due to huge dimensionality of the chemical space)[75]. In addition, these non-bonded interactions directly affect the thermodynamics properties of the system including enthalpy, free energy, and entropy which have special importance in structural biology[76]. It has been a daunting challenge to accurately describe the thermodynamics of these non-bonded interactions at the molecular level[76].

We demonstrate here that RexPoN FF can accurately predict the binding energies of water molecules against Nelfinavir structure (an HIV type-1 protease inhibitor). Here, we first calculated the binding energy, $\Delta E_{bind} = E_{total} - (E_{Nelfinavir} + E_{water})$, of a single molecule of water to Nelfinavir for several binding sites (see Figure 10) using QM. The non-periodic structure of Nelfinavir was initially optimized in QM (PBE-D3 DFT) using the 6-31G** basis set[77,78]. We then introduced a molecule of the water to the system and optimized the water using QM, while keeping Nelfinavir fixed. Next, we computed the ΔE_{bind} using RexPoN and Amber03 FFs[80]. For the RexPoN calculations, we started by just including the PQEq polarization and vdW non-bonded (E_{UNB}) energy terms. For PQEq we used parameters optimized based on the electric dipole energy scans for cyclohexane-based molecular structures[31]. For the atomic parameters of sulfur, we used a linear interpolation of atomic parameters of the elements from the same row (i.e. P, Cl, and Ar). For nitrogen we used the N (BP) parameters. For the parameters of water in Amber03 FF we used SPC water[81].

The results of binding energy calculations are summarized in Table 8. As shown, ΔE_{bind} of RexPoN is in reasonable agreement with ΔE_{bind} of QM with the root-mean-square error (RMSE) of 2.4 kcal/mol, much better than ΔE_{bind} of Amber03 (RMSE=6.1 kcal/mol). These results show that the PQEq model is able to account for most of short-range hydrogen bond (HB) contributions that are important in such polar systems.

However, it is well known that proteins need special HB corrections to account for the very polar nature of the amino acids. Thus, we considered an explicit term for the short-range HB interactions. For Nelfinavir these HB interactions are between water and oxygen (sites 1 to 5), nitrogen (site 9), and sulfur (site 8), as shown in Figure 10.

We use a similar Morse-type HB term as in Dreiding FF[15,79] given by

$$E_{HB}(r) = D_{hb}\{\exp[-2\alpha_{hb}(r - r_{hb})] - 2\exp[-\alpha_{hb}(r - r_{hb})]\}\cos^{n_{hb}}\theta \qquad (12)$$

where D_{hb}, α_{hb}, r_{hb}, and n_{hb} are the parameters to be determined. Our goal is to have only one set of global HB parameters that can work well for any kind of HB interactions such as the ones given in Figure 10. To do this we started with Dreiding HB energy and distance values (D_{hb} = 9.5 kcal/mol and r_{hb}=2.75 Å) from reference[15] and selected α_{hb} =5/r_{hb} =1.82 and n_{hb} =2 according to reference[79].

Then, we used the QM binding energy of sites 1, 8, and 9 (given in Table 8) as the training set and only modified D_{hb}, α_{hb}, and r_{hb} to get the best agreement with QM values. The optimized parameters are D_{hb} = 8.0 kcal/mol, α_{hb} = 1.72, r_{hb} = 2.92 Å, and n_{hb} = 2.

The results for ΔE_{bind} of RexPoN plus E_{HB} for different binding sites are given in Table 8. We find that using these HB parameters together with PQEq polarization and vdW non-bonded (E_{UNB}) energy terms provide excellent agreement between the computed RexPoN and QM (RMSE=0.5 kcal/mol).

Amber03 FF does not include an explicit term for the calculation of HB energy. Instead, the HB interactions are captured via modified 2-body vdW plus electrostatic energy terms. We wondered whether adding the HB energy term of RexPoN would help to improve the results of Amber03 FF. In Table 8 we show that addition of RexPoN HB term to Amber03 FF slightly improves the results but the difference between Amber03 FF and QM remains high with the RMSE of 4.0 kcal/mol, which is worse than RexPoN without HB corrections (RMSE=2.4 kcal/mol)

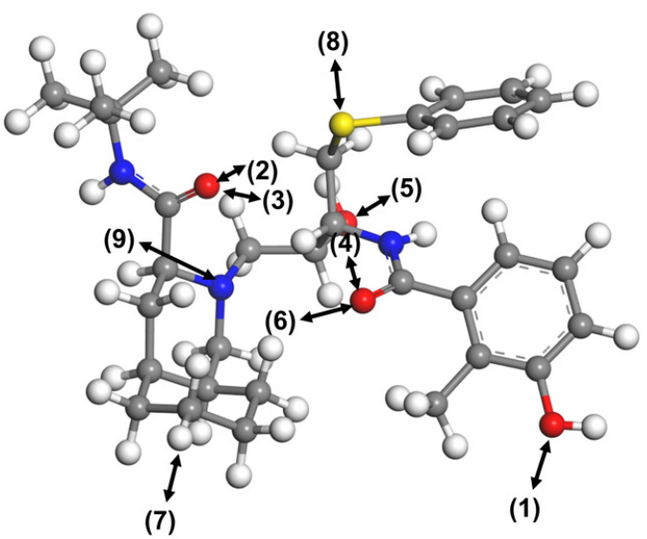

Figure 10. Binding sites of water molecule to Nelfinavir structure. The sites were selected to also study the hydrogen bond effects on the binding energies.

Table 7. Binding energy (ΔE_{bind}, kcal/mol) of water molecule to the various sites (shown in Figure 10) of Nelfinavir structure using QM, RexPoN, and Amber03 FFs with and without the HB (E_{HB}) corrections (Equation 12). The RMSE (kcal/mol) is calculated for all of the binding sites in each column.

Site	QM	RexPoN	Amber03	RexPoN+HB	Amber03+HB
1	-8.73	-3.12	-3.13	-8.46	-8.47
2	-11.16	-6.87	2.08	-12.43	-3.47
3	-12.77	-8.77	0.11	-15.20	-6.32
4	-15.66	-9.96	0.32	-17.89	-7.61
5	-16.63	-4.41	16.45	-14.52	6.34
6	-20.82	-8.31	0.61	-19.89	-10.97
7	-7.04	-3.75	0.90	-6.03	-1.37
8	-5.55	-4.06	-4.48	-5.44	-5.85
9	5.72	12.87	33.20	7.25	27.59
RMSE	-	2.4	6.1	0.5	4.0

VII. Conclusion

The goal of this paper is to report a new methodology aimed at defining all non-bonded components (vdW, electrostatics, hydrogen bonds) for use in force fields. These new non-bonded terms may be suitable for use in current FFs such as OPLS, AMBER, and CHARMM, but we have not tested this application because our main interest is for a new generation reactive RexPoN FF based only on accurate QM, such as the one we developed for water system[22,23]. Thus each component of the FF is defined separately based on direct QM energies or forces. This paper focuses on developing the vdW part of the RexPoN FF, using DFT-D3 calculations including dispersion corrections to obtain the energy-volume EOS of single element crystals. The use of single element data excludes polarization and electrostatics contributions, so that the DFT provides the vdW energy. In particular, we derived the vdW non-bonded potential parameters ($E_{PR\text{-}LD}$) for H, C, N, O, P, F, Cl, Br, I, He, Ne, Ar, Kr, Xe, and Rn, based on the DFT-D energy-volume EOS. These vdW non-bonded potentials are suitable to describe interatomic interactions for long- and short-range interactions.

In addition, we discovered that that the vdW potential curves extracted from EOS for the 6 noble gases lead to essentially identical curves, E_{UNB}, after scaling with just 3 parameters, D_e, R_e, and L. This suggests that this universal non-bonded curve (E_{UNB}) can be used for all atoms of the periodic table. This simplifies the task of obtaining vdW for the remainder of the periodic table, since we need only find ways to fit the trends in D_e, R_e, and L along the rows or columns.

We use PQEq model to describe polarization and electrostatics in various materials. PQEq uses Gaussian-shaped electron densities for atoms and dynamically updates the charge distribution and electron shell positions across the system. The important advantage of PQEq is that all parameters of the model are defined directly based on QM energy of electric probe dipoles with no vdW

contributions. The combination of $E_{PR\text{-}LD}$ (or E_{UNB}) with PQEq defines the dominant part of the non-bonded potential of RexPoN FF. Therefore, we make no assumptions to specify the contributions of vdW, electrostatics, and other components of the non-bonded potential to the total QM energy. In principle, this should provide transferability and accuracy of RexPoN FF for new systems and materials without the need to reoptimize the parameters for specific systems being studied. We validated the accuracy of $E_{PR\text{-}LD}$ and E_{UNB} for several systems including water system, energetic materials, and biological systems.

Supplementary Material

The supplementary material includes: computational details, description of the training set, comparison between universal non-bonded potential of RexPoN and other potentials, and melting point calculations for different isotopes of water.

Acknowledgements

SN was supported by the Joint Center for Artificial Photosynthesis, a DOE Energy Innovation Hub, supported through the Office of Science of the U.S. Department of Energy under Award No. DE-SC0004993. WAG was supported by the Computational Materials Sciences Program funded by the U.S. Department of Energy, Office of Science, Basic Energy Sciences, under Award Number DE-SC00014607. SZ was supported by the Office of Naval Research grants No. N00014-19-1-2081 and N00014-18-1-2155. JO was supported by the Ernest H. Swift and Arthur A. Noyes SURF Fellowships. The calculations were carried out on the Extreme Science and Engineering Discovery Environment (XSEDE), which is supported by National Science Foundation Grant Number ACI-1548562.

References

(1) Jorgensen, W. L.; Madura, J. D.; Swenson, C. J. Optimized Intermolecular Potential Functions for Liquid Hydrocarbons. *Journal of the American Chemical Society* **1984**, *106* (22), 6638–6646.

(2) Wang, J.; Wolf, R. M.; Caldwell, J. W.; Kollman, P. A.; Case, D. A. Development and Testing of a General Amber Force Field. *Journal of computational chemistry* **2004**, *25* (9), 1157–1174.

(3) MacKerell, A. D.; Bashford, D.; Bellott, M.; Dunbrack, R. L.; Evanseck, J. D.; Field, M. J.; Fischer, S.; Gao, J.; Guo, H.; Ha, S.; et al. All-Atom Empirical Potential for Molecular Modeling and Dynamics Studies of Proteins. *J. Phys. Chem. B* **1998**, *102* (18), 3586–3616. https://doi.org/10.1021/jp973084f.

(4) Abascal, J. L.; Vega, C. A General Purpose Model for the Condensed Phases of Water: TIP4P/2005. *The Journal of chemical physics* **2005**, *123* (23), 234505.

(5) Molinero, V.; Moore, E. B. Water Modeled as an Intermediate Element between Carbon and Silicon. *The Journal of Physical Chemistry B* **2008**, *113* (13), 4008–4016.

(6) Berendsen, H.; Grigera, J.; Straatsma, T. The Missing Term in Effective Pair Potentials. *Journal of Physical Chemistry* **1987**, *91* (24), 6269–6271.

(7) Jorgensen, W. L.; Chandrasekhar, J.; Madura, J. D.; Impey, R. W.; Klein, M. L. Comparison of Simple Potential Functions for Simulating Liquid Water. *The Journal of chemical physics* **1983**, *79* (2), 926–935.
(8) Naserifar, S.; Liu, L.; Goddard III, W. A.; Tsotsis, T. T.; Sahimi, M. Toward a Process-Based Molecular Model of SiC Membranes. 1. Development of a Reactive Force Field. *The Journal of Physical Chemistry C* **2013**, *117* (7), 3308–3319.
(9) Naserifar, S.; Goddard III, W. A.; Liu, L.; Tsotsis, T. T.; Sahimi, M. Toward a Process-Based Molecular Model of SiC Membranes. 2. Reactive Dynamics Simulation of the Pyrolysis of Polymer Precursor to Form Amorphous SiC. *The Journal of Physical Chemistry C* **2013**, *117* (7), 3320–3329.
(10) van Duin, A.; Verners, O.; Shin, Y.-K. Reactive Force Fields: Concepts of ReaxFF and Applications to High-Energy Materials. *International Journal of Energetic Materials and Chemical Propulsion* **2013**, *12* (2).
(11) Nielson, K. D.; Van Duin, A. C.; Oxgaard, J.; Deng, W.-Q.; Goddard, W. A. Development of the ReaxFF Reactive Force Field for Describing Transition Metal Catalyzed Reactions, with Application to the Initial Stages of the Catalytic Formation of Carbon Nanotubes. *The Journal of Physical Chemistry A* **2005**, *109* (3), 493–499.
(12) Mueller, J. E.; Van Duin, A. C.; Goddard III, W. A. Development and Validation of ReaxFF Reactive Force Field for Hydrocarbon Chemistry Catalyzed by Nickel. *The Journal of Physical Chemistry C* **2010**, *114* (11), 4939–4949.
(13) Rappe, A. K.; Casewit, C. J.; Colwell, K. S.; Goddard, W. A.; Skiff, W. M. UFF, a Full Periodic Table Force Field for Molecular Mechanics and Molecular Dynamics Simulations. *J. Am. Chem. Soc.* **1992**, *114* (25), 10024–10035. https://doi.org/10.1021/ja00051a040.
(14) Van Duin, A. C.; Dasgupta, S.; Lorant, F.; Goddard, W. A. ReaxFF: A Reactive Force Field for Hydrocarbons. *The Journal of Physical Chemistry A* **2001**, *105* (41), 9396–9409.
(15) Mayo, S. L.; Olafson, B. D.; Goddard, W. A. DREIDING: A Generic Force Field for Molecular Simulations. *Journal of Physical chemistry* **1990**, *94* (26), 8897–8909.
(16) Vedani, A.; Huhta, D. W. A New Force Field for Modeling Metalloproteins. *Journal of the American Chemical Society* **1990**, *112* (12), 4759–4767.
(17) Allinger, N. L. Conformational Analysis. 130. MM2. A Hydrocarbon Force Field Utilizing V1 and V2 Torsional Terms. *Journal of the American Chemical Society* **1977**, *99* (25), 8127–8134.
(18) Allinger, N. L.; Yuh, Y. H.; Lii, J. H. Molecular Mechanics. The MM3 Force Field for Hydrocarbons. 1. *Journal of the American Chemical Society* **1989**, *111* (23), 8551–8566.
(19) Borodin, O. Polarizable Force Field Development and Molecular Dynamics Simulations of Ionic Liquids. *J. Phys. Chem. B* **2009**, *113* (33), 11463–11478. https://doi.org/10.1021/jp905220k.
(20) Halgren, T. A. Merck Molecular Force Field. I. Basis, Form, Scope, Parameterization, and Performance of MMFF94. *Journal of computational chemistry* **1996**, *17* (5–6), 490–519.
(21) Ponder, J. W.; Wu, C.; Ren, P.; Pande, V. S.; Chodera, J. D.; Schnieders, M. J.; Haque, I.; Mobley, D. L.; Lambrecht, D. S.; DiStasio, R. A.; et al. Current Status of the AMOEBA Polarizable Force Field. *J. Phys. Chem. B* **2010**, *114* (8), 2549–2564. https://doi.org/10.1021/jp910674d.
(22) Naserifar, S.; Goddard, W. A. Liquid Water Is a Dynamic Polydisperse Branched Polymer. *Proceedings of the National Academy of Sciences* **2019**, *116* (6), 1998–2003.

(23) Naserifar, S.; Goddard III, W. A. The Quantum Mechanics-Based Polarizable Force Field for Water Simulations. *The Journal of chemical physics* **2018**, *149* (17), 174502.
(24) Medders, G. R.; Babin, V.; Paesani, F. Development of a "First-Principles" Water Potential with Flexible Monomers. III. Liquid Phase Properties. *Journal of chemical theory and computation* **2014**, *10* (8), 2906–2910.
(25) Bukowski, R.; Szalewicz, K.; Groenenboom, G. C.; van der Avoird, A. Polarizable Interaction Potential for Water from Coupled Cluster Calculations. I. Analysis of Dimer Potential Energy Surface. *The Journal of chemical physics* **2008**, *128* (9), 094313.
(26) Ponder, J. W.; Case, D. A. Force Fields for Protein Simulations. In *Advances in protein chemistry*; Elsevier, 2003; Vol. 66, pp 27–85.
(27) Cox, S.; Williams, D. Representation of the Molecular Electrostatic Potential by a Net Atomic Charge Model. *Journal of Computational chemistry* **1981**, *2* (3), 304–323.
(28) Williams, D. E. Representation of the molecular electrostatic potential by atomic multipole and bond dipole models. *Journal of Computational Chemistry* **1988**, *9* (7), 745–763. https://doi.org/10.1002/jcc.540090705.
(29) Cusachs, L. C.; Politzer, P. On the Problem of Defining the Charge on an Atom in a Molecule. *Chemical Physics Letters* **1968**, *1* (11), 529–531.
(30) Löwdin, P.-O. On the Nonorthogonality Problem. In *Advances in quantum chemistry*; Elsevier, 1970; Vol. 5, pp 185–199.
(31) Naserifar, S.; Brooks, D. J.; Goddard, W. A.; Cvicek, V. Polarizable Charge Equilibration Model for Predicting Accurate Electrostatic Interactions in Molecules and Solids. *The Journal of Chemical Physics* **2017**, *146* (12), 124117. https://doi.org/10.1063/1.4978891.
(32) Oppenheim, J. J.; Naserifar, S.; Goddard III, W. A. Extension of the Polarizable Charge Equilibration Model to Higher Oxidation States with Applications to Ge, As, Se, Br, Sn, Sb, Te, I, Pb, Bi, Po, and At Elements. *J. Phys. Chem. A* **2018**, *122* (2), 639–645. https://doi.org/10.1021/acs.jpca.7b06612.
(33) Kwon, S.; Naserifar, S.; Lee, H. M.; Goddard, W. A. Polarizable Charge Equilibration Model for Transition-Metal Elements. *J. Phys. Chem. A* **2018**, *122* (48), 9350–9358. https://doi.org/10.1021/acs.jpca.8b07290.
(34) Grimme, S. Semiempirical GGA-Type Density Functional Constructed with a Long-Range Dispersion Correction. *Journal of computational chemistry* **2006**, *27* (15), 1787–1799.
(35) Grimme, S.; Antony, J.; Ehrlich, S.; Krieg, H. A Consistent and Accurate Ab Initio Parametrization of Density Functional Dispersion Correction (DFT-D) for the 94 Elements H-Pu. *The Journal of chemical physics* **2010**, *132* (15), 154104.
(36) Loubeyre, P.; LeToullec, R.; Hausermann, D.; Hanfland, M.; Hemley, R.; Mao, H.; Finger, L. X-Ray Diffraction and Equation of State of Hydrogen at Megabar Pressures. *Nature* **1996**, *383* (6602), 702.
(37) Kohanoff, J.; Scandolo, S.; Chiarotti, G. L.; Tosatti, E. Solid Molecular Hydrogen: The Broken Symmetry Phase. *Physical review letters* **1997**, *78* (14), 2783.
(38) Städele, M.; Martin, R. M. Metallization of Molecular Hydrogen: Predictions from Exact-Exchange Calculations. *Physical Review Letters* **2000**, *84* (26), 6070.
(39) Barrett, C.; Meyer, L.; Wasserman, J. Antiferromagnetic and Crystal Structures of Alpha-Oxygen. *The Journal of Chemical Physics* **1967**, *47* (2), 592–597.
(40) Freiman, Y. A.; Jodl, H.-J. Solid Oxygen. *Physics Reports* **2004**, *401* (1–4), 1–228.
(41) Somiya, S. *Handbook of Advanced Ceramics: Materials, Applications, Processing, and Properties*; Academic press, 2013.

(42) Tonkov, E. Y.; Ponyatovsky, E. *Phase Transformations of Elements under High Pressure*; CRC press, 2004.
(43) Brown, A.; Rundqvist, S. Refinement of the Crystal Structure of Black Phosphorus. *Acta Crystallographica* **1965**, *19* (4), 684–685.
(44) Meyer, L.; Barrett, C.; Greer, S. C. Crystal Structure of α-Fluorine. *The Journal of Chemical Physics* **1968**, *49* (4), 1902–1907.
(45) Powell, B.; Heal, K.; Torrie, B. The Temperature Dependence of the Crystal Structures of the Solid Halogens, Bromine and Chlorine. *Molecular Physics* **1984**, *53* (4), 929–939.
(46) Ibberson, R.; Moze, O.; Petrillo, C. High Resolution Neutron Powder Diffraction Studies of the Low Temperature Crystal Structure of Molecular Iodine (I2). *Molecular Physics* **1992**, *76* (2), 395–403.
(47) Pollack, G. L. The Solid State of Rare Gases. *Reviews of Modern Physics* **1964**, *36* (3), 748.
(48) Becke, A. D. Density-functional Thermochemistry. III. The Role of Exact Exchange. *The Journal of Chemical Physics* **1993**, *98* (7), 5648–5652. https://doi.org/10.1063/1.464913.
(49) Lee, C.; Yang, W.; Parr, R. G. Development of the Colle-Salvetti Correlation-Energy Formula into a Functional of the Electron Density. *Physical review B* **1988**, *37* (2), 785.
(50) Grimme, S.; Ehrlich, S.; Goerigk, L. Effect of the Damping Function in Dispersion Corrected Density Functional Theory. *Journal of computational chemistry* **2011**, *32* (7), 1456–1465.
(51) Liu, Y.; Goddard III, W. A. First-Principles-Based Dispersion Augmented Density Functional Theory: From Molecules to Crystals. *The Journal of Physical Chemistry Letters* **2010**, *1* (17), 2550–2555.
(52) Kim, H.; Choi, J.-M.; Goddard III, W. A. Universal Correction of Density Functional Theory to Include London Dispersion (up to Lr, Element 103). *The journal of physical chemistry letters* **2012**, *3* (3), 360–363.
(53) Rose, J. H.; Smith, J. R.; Ferrante, J. Universal Features of Bonding in Metals. *Physical review B* **1983**, *28* (4), 1835.
(54) Varshni, Y. P. Comparative Study of Potential Energy Functions for Diatomic Molecules. *Reviews of Modern Physics* **1957**, *29* (4), 664.
(55) Plimpton, S. Fast Parallel Algorithms for Short-Range Molecular Dynamics. *Journal of Computational Physics* **1995**, *117* (1), 1–19. https://doi.org/10.1006/jcph.1995.1039.
(56) Axilrod, B.; Teller, E. Interaction of the van Der Waals Type between Three Atoms. *The Journal of Chemical Physics* **1943**, *11* (6), 299–300.
(57) Lin, S.-T.; Maiti, P. K.; Goddard III, W. A. Two-Phase Thermodynamic Model for Efficient and Accurate Absolute Entropy of Water from Molecular Dynamics Simulations. *The Journal of Physical Chemistry B* **2010**, *114* (24), 8191–8198.
(58) Pascal, T. A.; Lin, S.-T.; Goddard III, W. A. Thermodynamics of Liquids: Standard Molar Entropies and Heat Capacities of Common Solvents from 2PT Molecular Dynamics. *Physical chemistry chemical physics* **2011**, *13* (1), 169–181.
(59) Pascal, T. A.; Goddard III, W. A. Interfacial Thermodynamics of Water and Six Other Liquid Solvents. *The Journal of Physical Chemistry B* **2014**, *118* (22), 5943–5956.
(60) Schneider, T.; Stoll, E. Molecular-Dynamics Study of a Three-Dimensional One-Component Model for Distortive Phase Transitions. *Physical Review B* **1978**, *17* (3), 1302.
(61) Lide, D. R.; Milne, G. W. A. *CRC Handbook of Data on Organic Compounds*; CRC Press, 1993.

(62) Pagoria, P. F.; Lee, G. S.; Mitchell, A. R.; Schmidt, R. D. A Review of Energetic Materials Synthesis. *Thermochimica Acta* **2002**, *384* (1–2), 187–204.
(63) Naserifar, S.; Zybin, S.; Ye, C.-C.; Goddard III, W. A. Prediction of Structures and Properties of 2, 4, 6-Triamino-1, 3, 5-Triazine-1, 3, 5-Trioxide (MTO) and 2, 4, 6-Trinitro-1, 3, 5-Triazine-1, 3, 5-Trioxide (MTO3N) Green Energetic Materials from DFT and ReaxFF Molecular Modeling. *Journal of Materials Chemistry A* **2016**, *4* (4), 1264–1276.
(64) Akhavan, J. *The Chemistry of Explosives*; Royal Society of Chemistry, 2011.
(65) Russell, T. P.; Miller, P. J.; Piermarini, G. J.; Block, S. Pressure/Temperature Phase Diagram of Hexanitrohexaazaisowurtzitane. *J. Phys. Chem.* **1993**, *97* (9), 1993–1997. https://doi.org/10.1021/j100111a043.
(66) Foltz, M. F.; Coon, C. L.; Garcia, F.; Nichols III, A. L. The Thermal Stability of the Polymorphs of Hexanitrohexaazaisowurtzitane, Part I. *Propellants, Explosives, Pyrotechnics* **1994**, *19* (1), 19–25.
(67) Foltz, M. F.; Coon, C. L.; Garcia, F.; Nichols III, A. L. The Thermal Stability of the Polymorphs of Hexanitrohexaazaisowurtzitane, Part II. *Propellants, explosives, pyrotechnics* **1994**, *19* (3), 133–144.
(68) Sorescu, D. C.; Rice, B. M. Theoretical Predictions of Energetic Molecular Crystals at Ambient and Hydrostatic Compression Conditions Using Dispersion Corrections to Conventional Density Functionals (DFT-D). *The Journal of Physical Chemistry C* **2010**, *114* (14), 6734–6748.
(69) Jorgensen, W. L.; Maxwell, D. S.; Tirado-Rives, J. Development and Testing of the OPLS All-Atom Force Field on Conformational Energetics and Properties of Organic Liquids. *J. Am. Chem. Soc.* **1996**, *118* (45), 11225–11236. https://doi.org/10.1021/ja9621760.
(70) Banks, J. L.; Beard, H. S.; Cao, Y.; Cho, A. E.; Damm, W.; Farid, R.; Felts, A. K.; Halgren, T. A.; Mainz, D. T.; Maple, J. R.; et al. Integrated Modeling Program, Applied Chemical Theory (IMPACT). *Journal of computational chemistry* **2005**, *26* (16), 1752–1780.
(71) Bowers, K. J.; Chow, D. E.; Xu, H.; Dror, R. O.; Eastwood, M. P.; Gregersen, B. A.; Klepeis, J. L.; Kolossvary, I.; Moraes, M. A.; Sacerdoti, F. D.; et al. Scalable Algorithms for Molecular Dynamics Simulations on Commodity Clusters. In *SC'06: Proceedings of the 2006 ACM/IEEE Conference on Supercomputing*; IEEE, 2006; pp 43–43.
(72) Sinditskii, V.; Egorshev, V. Y.; Serushkin, V.; Levshenkov, A.; Berezin, M.; Filatov, S.; Smirnov, S. Evaluation of Decomposition Kinetics of Energetic Materials in the Combustion Wave. *Thermochimica Acta* **2009**, *496* (1–2), 1–12.
(73) Dorofeeva, O. V.; Suntsova, M. A. Enthalpy of Formation of CL-20. *Computational and Theoretical Chemistry* **2015**, *1057*, 54–59.
(74) Zeman, S.; Krupka, M. New Aspects of Impact Reactivity of Polynitro Compounds, Part III. Impact Sensitivity as a Function of the Imtermolecular Interactions. *Propellants, Explosives, Pyrotechnics: An International Journal Dealing with Scientific and Technological Aspects of Energetic Materials* **2003**, *28* (6), 301–307.
(75) MacKerell Jr, A. D. Empirical Force Fields for Biological Macromolecules: Overview and Issues. *Journal of computational chemistry* **2004**, *25* (13), 1584–1604.
(76) Meirovitch, H.; Cheluvaraja, S.; White, R. P. Methods for Calculating the Entropy and Free Energy and Their Application to Problems Involving Protein Flexibility and Ligand Binding. *Current Protein and Peptide Science* **2009**, *10* (3), 229–243.

(77) Ditchfield, R.; Hehre, W. J.; Pople, J. A. Self-Consistent Molecular-Orbital Methods. IX. An Extended Gaussian-Type Basis for Molecular-Orbital Studies of Organic Molecules. *The Journal of Chemical Physics* **1971**, *54* (2), 724–728.
(78) Hehre, W.; Pople, J. Self-Consistent Molecular Orbital Methods. XIII. An Extended Gaussian-Type Basis for Boron. *The Journal of Chemical Physics* **1972**, *56* (8), 4233–4234.
(79) Liu, Y.; Bryantsev, V. S.; Diallo, M. S.; Goddard Iii, W. A. PAMAM Dendrimers Undergo PH Responsive Conformational Changes without Swelling. *Journal of the American Chemical Society* **2009**, *131* (8), 2798–2799.
(80) Duan, Y.; Wu, C.; Chowdhury, S.; Lee, M. C.; Xiong, G.; Zhang, W.; Yang, R.; Cieplak, P.; Luo, R.; Lee, T.; et al. A Point-Charge Force Field for Molecular Mechanics Simulations of Proteins Based on Condensed-Phase Quantum Mechanical Calculations. *Journal of computational chemistry* **2003**, *24* (16), 1999–2012.
(81) Berendsen, H.; Postma, J.; Van Gunsteren, W.; Hermans, a J. *Intermolecular Forces*; Reidel, Dordrecht Jerusalem, Israel, 1981.

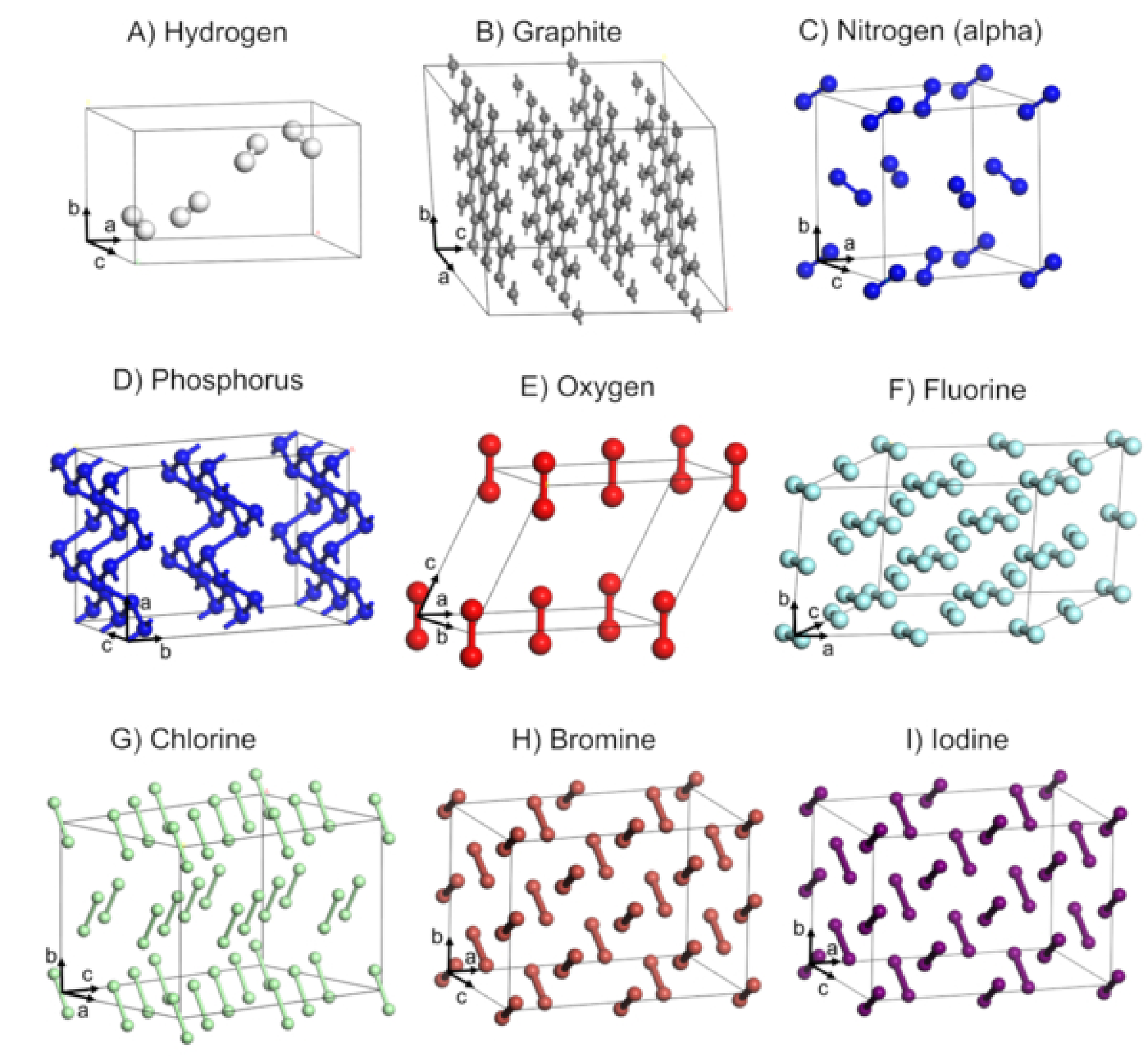
A) Hydrogen
B) Graphite
C) Nitrogen (alpha)
D) Phosphorus
E) Oxygen
F) Fluorine
G) Chlorine
H) Bromine
I) Iodine

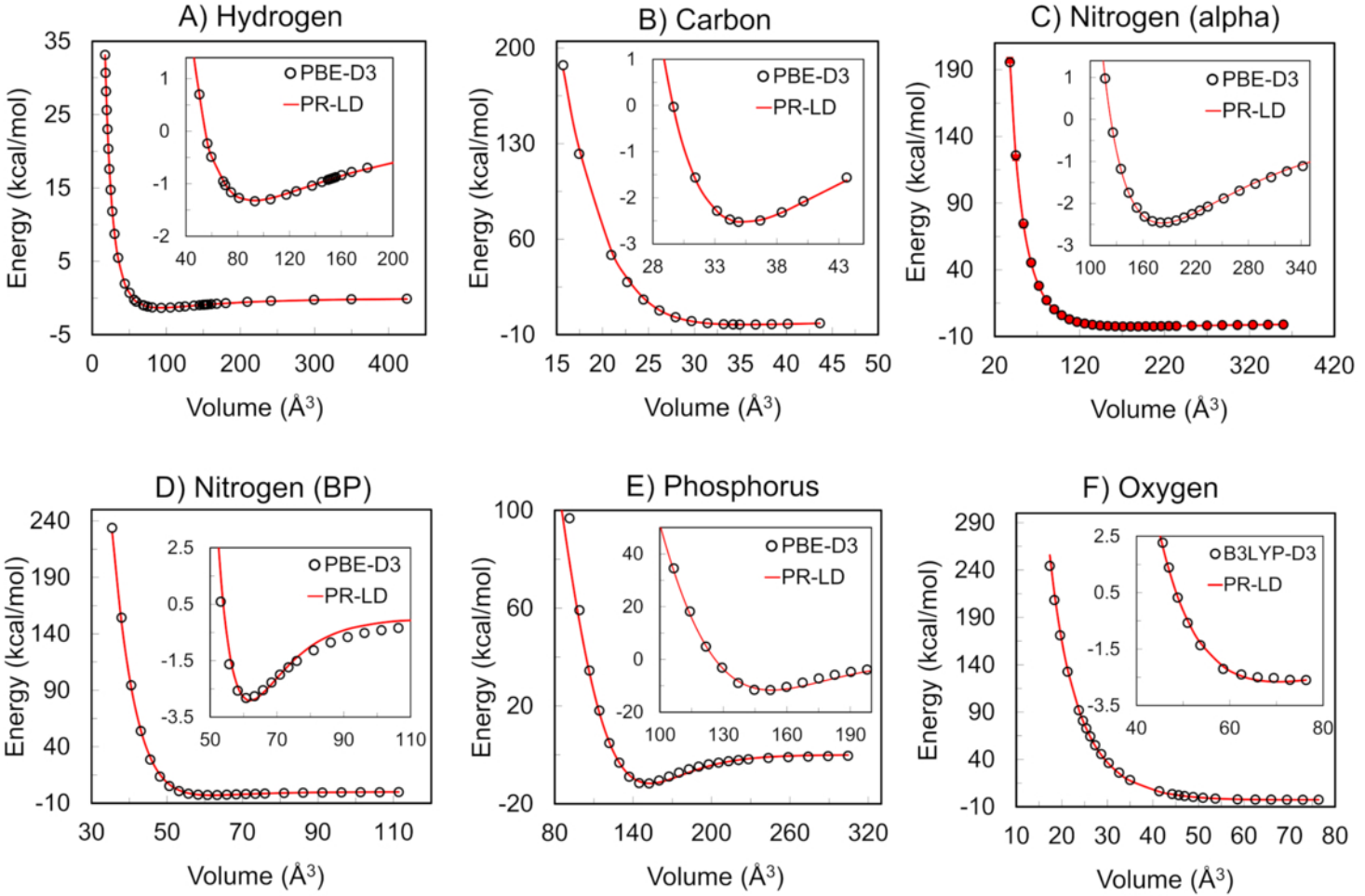
A) Hydrogen
B) Carbon
C) Nitrogen (alpha)
D) Nitrogen (BP)
E) Phosphorus
F) Oxygen
Energy (kcal/mol)
Volume (Å3)
PBE-D3
PR-LD
B3LYP-D3

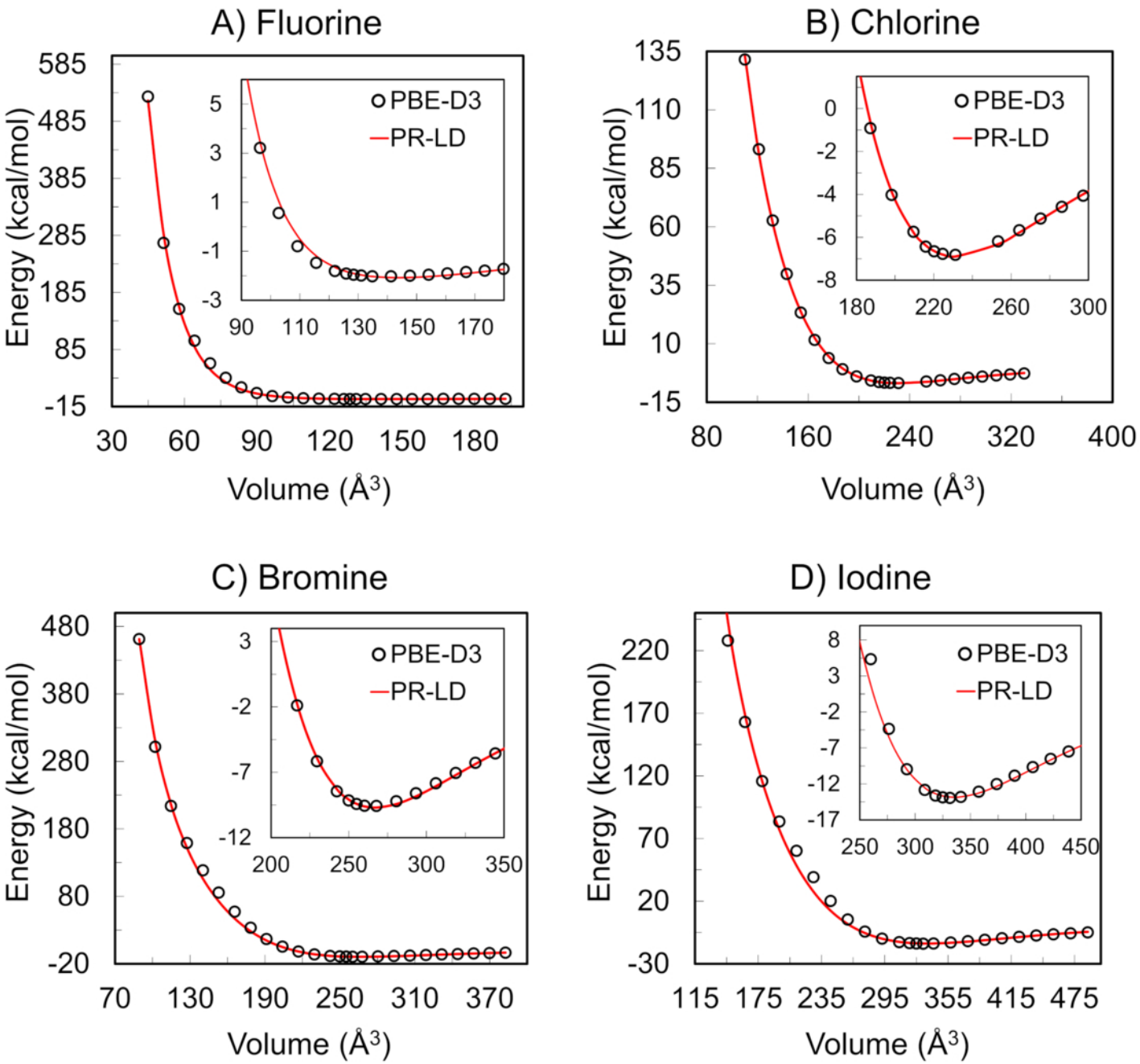
A) Fluorine
B) Chlorine
C) Bromine
D) Iodine
Energy (kcal/mol)
Volume (Å3)
PBE-D3
PR-LD

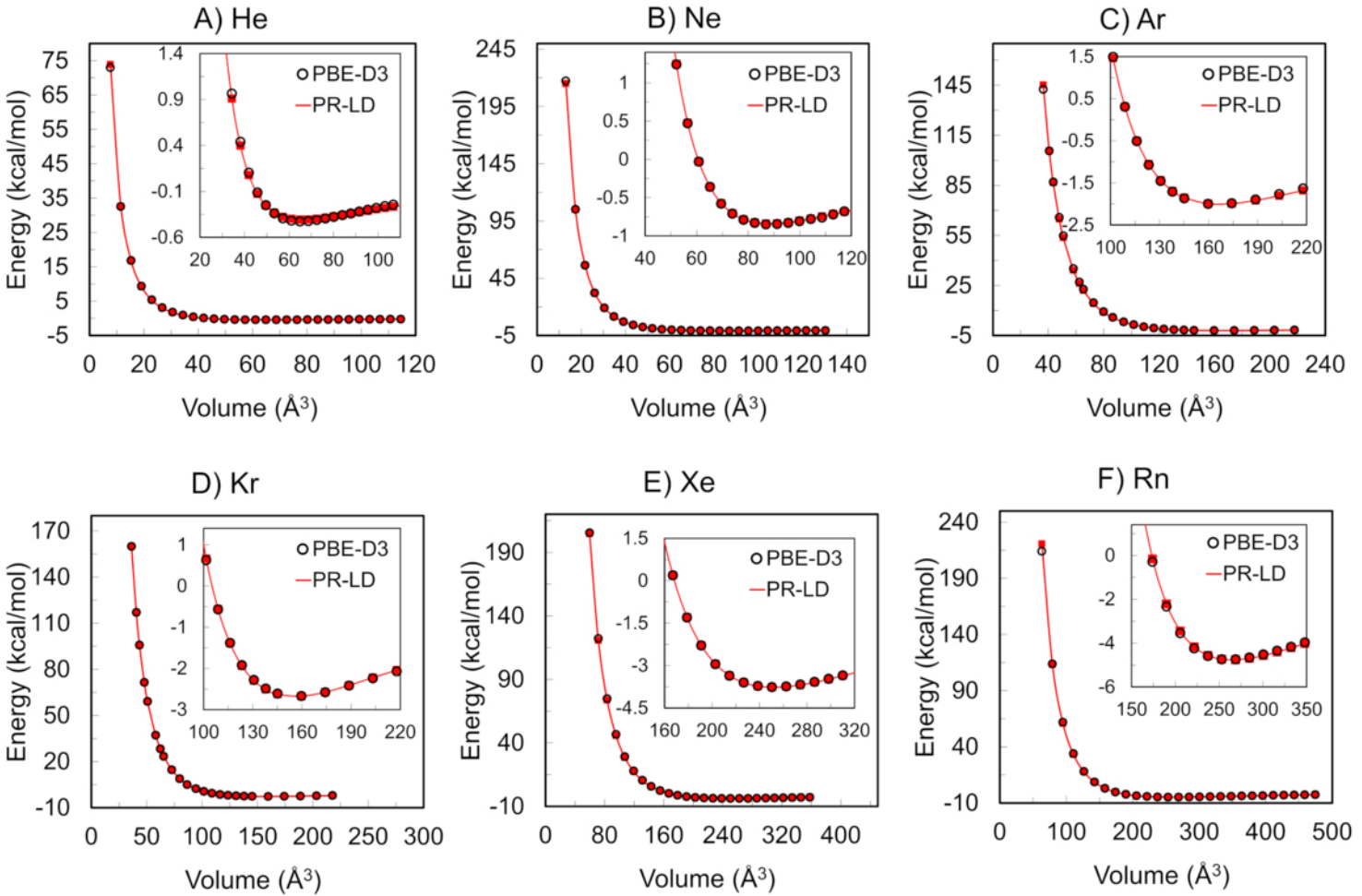
A) He
B) Ne
C) Ar
D) Kr
E) Xe
F) Rn
Energy (kcal/mol)
Volume (Å3)
PBE-D3
PR-LD

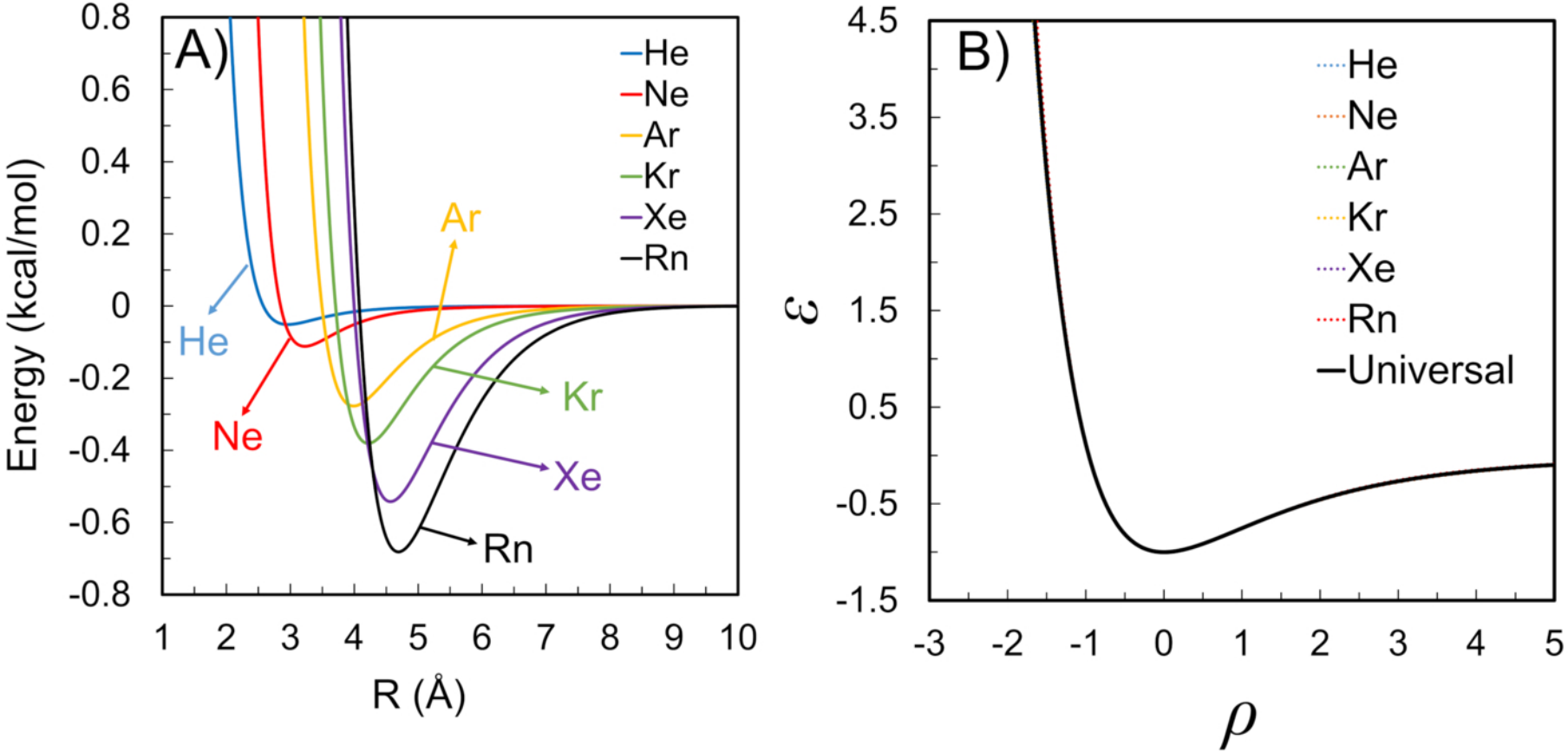
A)
Energy (kcal/mol)
R (Å)
He
Ne
Ar
Kr
Xe
Rn
B)
ε
ρ
Universal

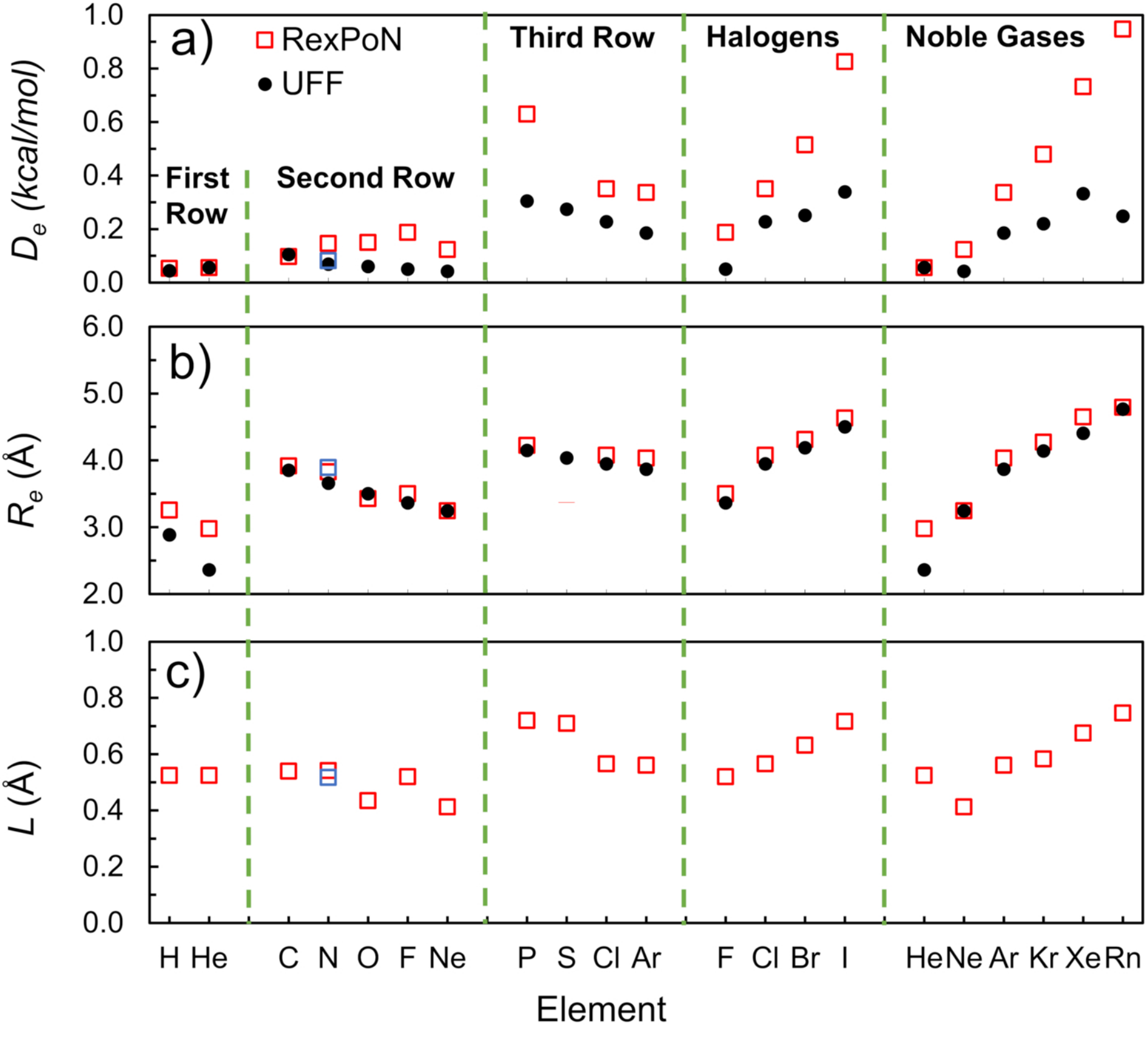
a)
RexPoN
UFF
First Row
Second Row
Third Row
Halogens
Noble Gases
D_e (kcal/mol)
1.0
0.8
0.6
0.4
0.2
0.0
b)
R_e (Å)
6.0
5.0
4.0
3.0
2.0
c)
L (Å)
1.0
0.8
0.6
0.4
0.2
0.0
H He C N O F Ne P S Cl Ar F Cl Br I He Ne Ar Kr Xe Rn
Element

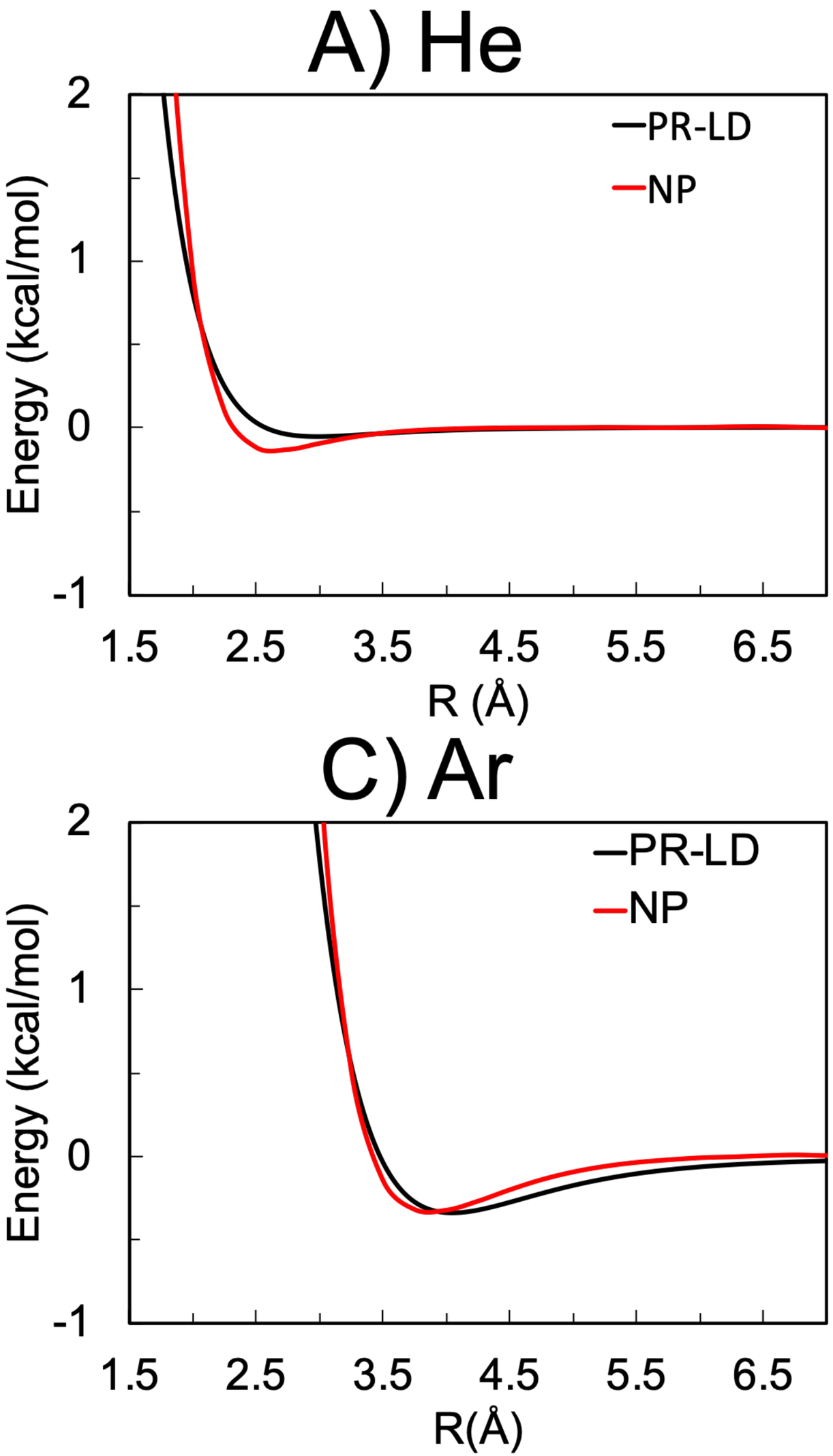
A) He
PR-LD
NP
Energy (kcal/mol)
2
1
0
-1
1.5
2.5
3.5
4.5
5.5
6.5
R (Å)

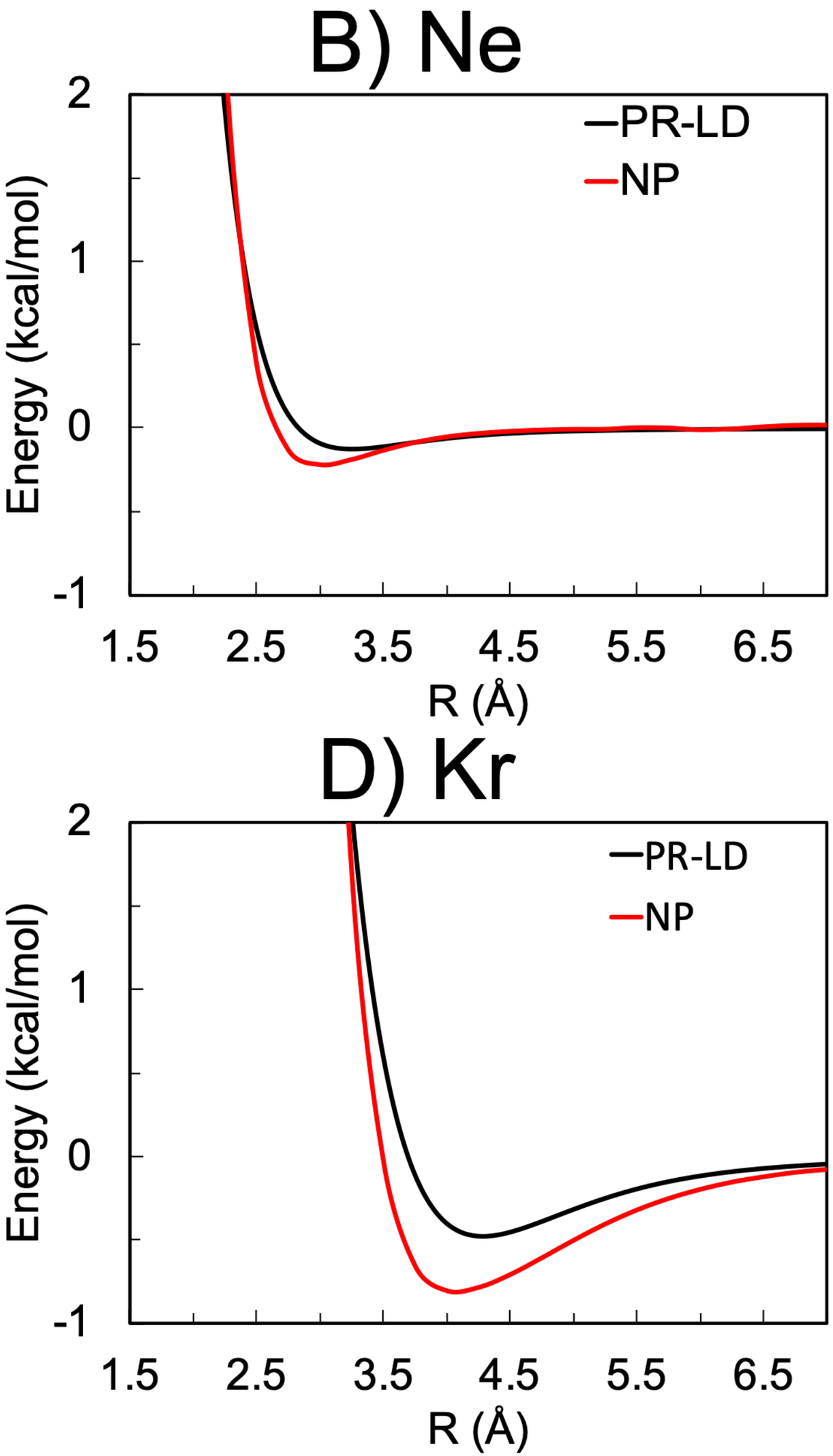
B) Ne
PR-LD
NP
Energy (kcal/mol)
2
1
0
-1
1.5
2.5
3.5
4.5
5.5
6.5
R (Å)

C) Ar
PR-LD
NP
Energy (kcal/mol)
2
1
0
-1
1.5
2.5
3.5
4.5
5.5
6.5
R(Å)

D) Kr
PR-LD
NP
Energy (kcal/mol)
2
1
0
-1
1.5
2.5
3.5
4.5
5.5
6.5
R (Å)

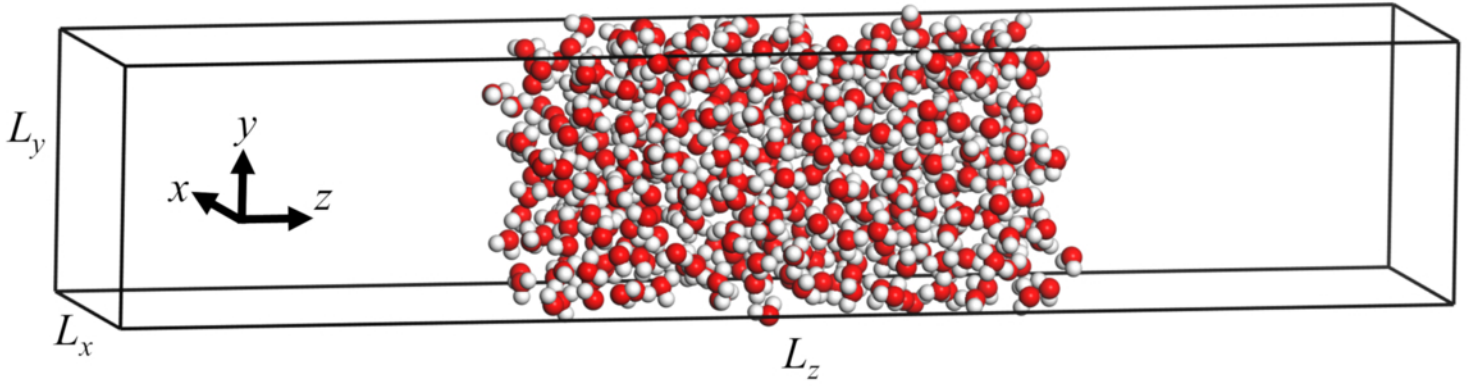
L_y
y
x
z
L_x
L_z

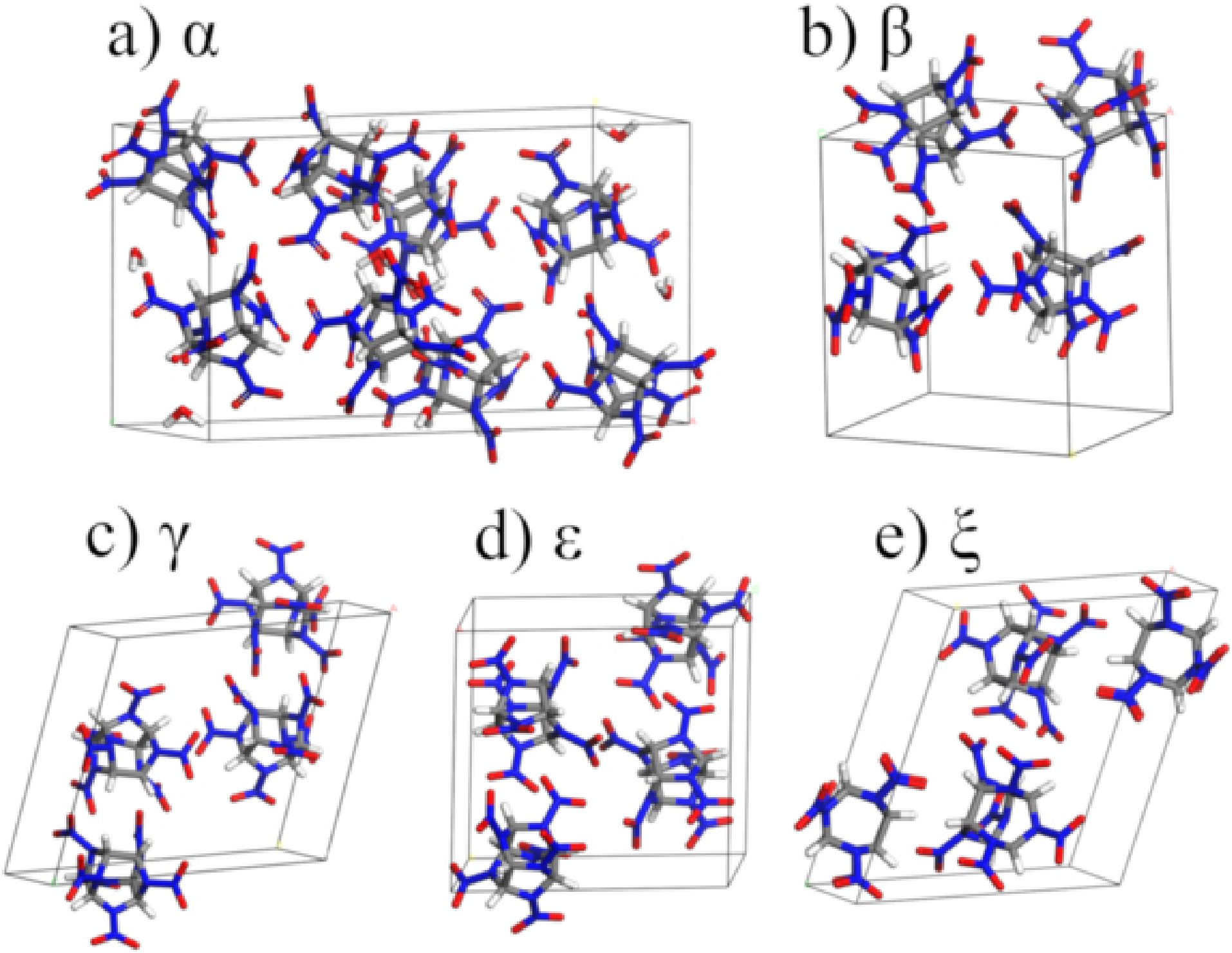
a) α
b) β
c) γ
d) ε
e) ξ

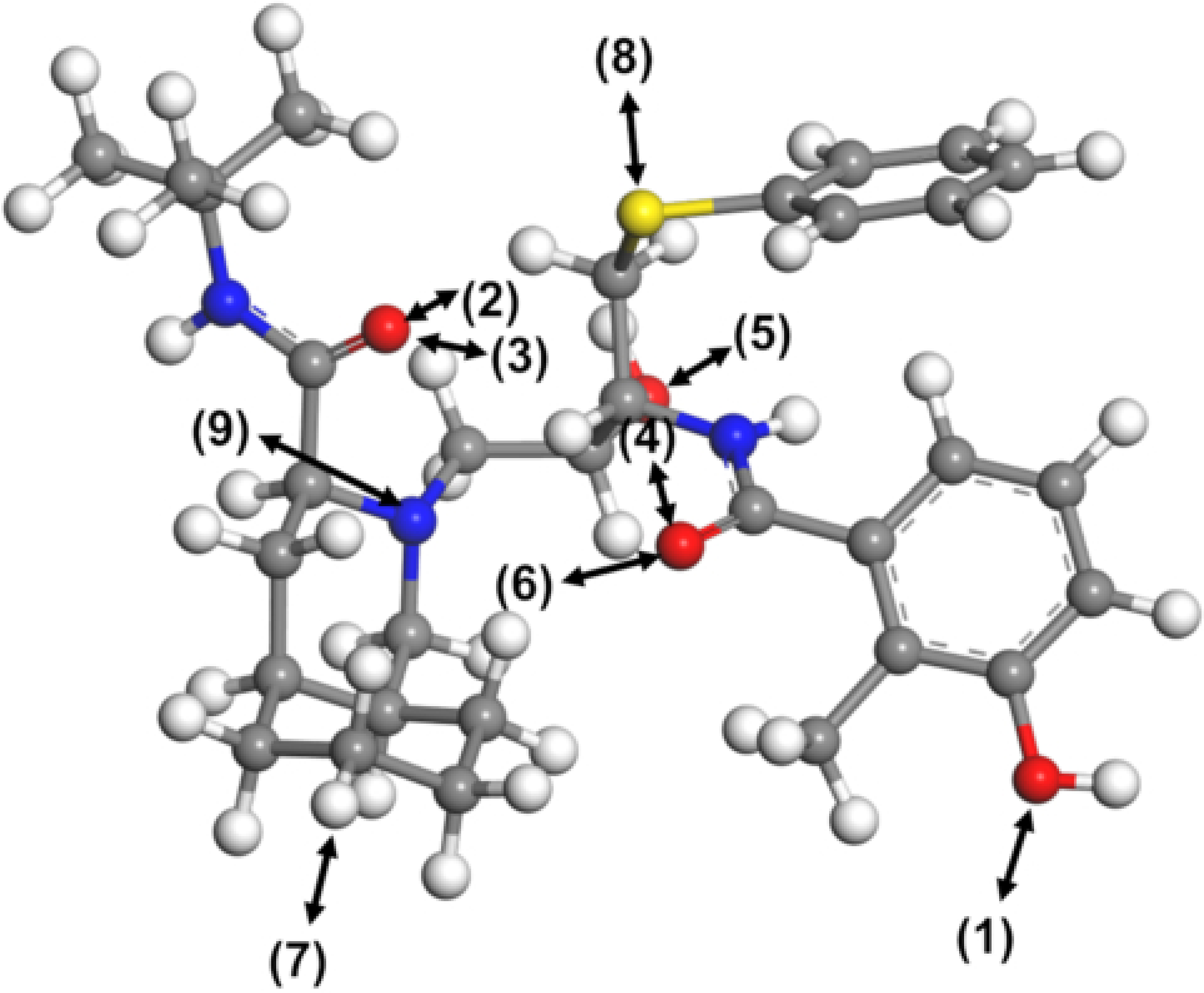
(8)
(2)
(3)
(5)
(9)
(4)
(6)
(7)
(1)